High-Resolution Continuous-Scan Beamforming

David Morata* and Dimitri Papamoschou.†
University of California, Irvine, Irvine, CA, 92607

The paper adapts the delay-and-sum beamforming method and related deconvolution techniques for microphone phased arrays comprising fixed and continuously-scanning sensors. Processing of the non-stationary signals introduced by the scanning sensors requires division of all the signals into quasi-stationary blocks and application of a frequency-dependent window within each block. Three distinct approaches are developed: application of delay-and-sum to each block of the divided signals followed by assembly of the outputs of the blocks; a cross-spectral matrix completion process; and a partial fields decomposition method. The last two approaches result in a unified cross-spectral matrix that facilitates deconvolution of the array output. The methodologies are applied to a synthetic noise source and to a supersonic under-expanded jet that presented the phenomenon of screech. Introduction of a single scanning sensor to a far-field array comprising 13 fixed sensors improves significantly the fidelity of beamforming. The deconvolved images of the jet noise source resolve fine shock-cell features whose dimensions are similar to those imaged by optical techniques in past investigations.

Nomenclature

D	=	jet diameter
$\mathbf{e}$	=	steering vector
f	=	cyclic frequency
$\mathbf{G}$	=	cross spectral matrix
J	=	number of non-repeating elements of cross-spectral submatrices
K	=	total number of blocks
L	=	array linear aperture
$\mathcal{M}$	=	number of microphones
$\mathcal{N}_x$	=	number of divisions of the region of interest
N_{FFT}	=	size of Fast Fourier Transform
P_m	=	Fourier Transform of $p_m(t)$

*Graduate Student Researcher, Mechanical and Aerospace Engineering, dmoratac@uci.edu, Member AIAA.
†Professor, Mechanical and Aerospace Engineering, dpapamos@uci.edu, Fellow AIAA.

r	=	iteration step
R	=	residual error; mean sensor distance from source origin
s	=	delay-and-sum signal in time domain
S	=	delay-and-sum signal in frequency domain
$\mathcal{S}$	=	point spread function
t	=	time
T	=	block duration
U	=	fully-expanded jet velocity
V	=	sensor speed
w	=	weight
W	=	modified weight
x	=	axial coordinate
X	=	source location
y	=	transverse coordinate
Y	=	array output
α	=	derivative given by Eq. 11
β	=	angle of sensor trajectory
ϵ	=	error
θ	=	polar angle relative to jet axis
κ	=	spatial wavenumber
λ	=	acoustic wavelength
ℓ	=	source-sensor distance
τ	=	source-sensor travel time
ξ	=	coordinate along the source line
ω	=	angular frequency
ω'	=	Doppler-shifted frequency

Subscripts

k	=	block index
m, n	=	microphone indices
s	=	scanning sensor
f	=	fixed sensor

I. Introduction

Beamforming has become a standard tool in aeroacoustic experiments. Its widest application uses the delay-and-sum (DAS) technique to electronically steer signals sampled simultaneously by an array of sensors to the region of interest [1, 2]. The DAS array output is a convolution between the source distribution and the array point spread function (PSF). The ideal PSF has a narrowly focused main lobe and suppressed sidelobes. Approaching this ideal generally requires a large aperture and a dense arrangement of closely-spaced microphones. A large aperture may be counter-productive when studying the emission of sources whose character is directional, e.g., the noise from turbulent jets. A large number of sensors, and their accompanying infrastructure, can be prohibitively expensive. In an effort to enhance the spatial resolution of DAS-based beamforming past research has considered shading algorithms and non-uniform microphone weightings [1, 3]. These techniques attenuate the effect of the sidelobes of the point spread function up to a certain level but the resulting image might still not be of the desired resolution. Mitigating the effect of the PSF can also be addressed via deconvolution methods[3–8]. The probability of success of deconvolution depends strongly on the quality of the PSF; a highly complex PSF will generally lead to failure [9, 10].

In recent years there has been increasing interest in arrays that include continuously-scanning sensors. The main attractiveness is the potential of high spatial resolution with a limited number of sensors. The continuous-scan approach can be considered as an extension of the stop-and-start (fixed indexing) method of Ref. Lee and Bolton [11] and has found applications in acoustic holography [12–14], order tracking [15] and beamforming [16]. In certain configurations, order-of-magnitude reduction in acquisition time, with same measurement quality, has been achieved in comparison to fixed-position sensors [17] or fixed indexing [18]. Reference [19] introduced a direct spectral estimation approach to obtain the noise source distribution from microphone arrays that contained continuously-scanning sensors. The work also studied the non-stationarity introduced by the motion of the scanning sensors and used the Wigner-Ville spectral estimator to quantify its effects. Suppression of those effects involved the division of the signals into quasi-stationary blocks and application of a frequency-dependent window within each block. Optimization of the signal processing, including block division, has been addressed in Ref. [20]. On a separate but related subject, there has been significant progress on the treatment of non-synchronous microphone measurements [21–25]. The associated methods will play a role here in the development of high-resolution methods to image the noise source.

This paper investigates the incorporation of the continuous-scan paradigm into the DAS-based beamforming and associated deconvolution methods. As with the direct spectral estimation method, suppression of the effects of non-stationarity is critical and involves the same signal processing steps outlined above. Three distinct approaches are introduced. The first method applies DAS to each block of the divided signals, then assembles the array outputs of

the blocks in a way that prevents overlap. A drawback is the lack of a complete cross-spectral matrix (CSM) that encompasses the finely resolved sensor positions enabled by the continuous-scan paradigm.A complete CSM is desired in order to use adaptive methods and to adopt current deconvolution methods in a straightforward fashion. Thus, two additional methodologies are presented towards this goal. They involve a cross-spectral matrix completion (CSMC) process and a partial fields decomposition (PFD) technique. Several deconvolution techniques are then used to further sharpen the noise source maps obtained through CSMC and PFD. The methodologies are first applied to a synthetic noise source to evaluate the performance of the different continuous-scan methods. Then, a supersonic underexpanded jet that presented the phenomenon of screech is investigated. This aeroacoustic source is of interest given its intricate flow field [26–31] containing shock cells in combination with large and fine scale turbulence structures interacting with them, and creating additional noise sources.

The paper is structured as follows. First, the features and challenges of signal division are introduced. DAS beamfoming using fixed sensors is briefly reviewed as background. A direct extension of DAS to an array comprising fixed and continuously-scanning sensors is developed, relying on cross-spectral submatrices (CSSM) to construct the array output. This is followed by two approaches for obtaining the missing elements of a unified CSM: a cross-spectral matrix completion (CSMC) method and a partial fields decomposition (PFD) technique. Deconvolution is briefly reviewed and extended to the continuous-scan paradigm. The experimental setup is described next, including the microphone array and the noise sources of interest. The results and conclusions sections follow. An earlier version of this paper appeared in the AIAA 2022 SciTech Forum [32].

II. Methodology

A. Problem Setup

Figure 1 outlines the essential elements of the problem studied here. Consistent with the general approach used in several past studies (e.g., [2]), the jet noise source is approximated by a one-dimensional distribution, along the jet axis, of equivalent sources as viewed by a far-field observer. The sources are uncorrelated and their distribution is denoted $q(\xi, t)$, where ξ is the source coordinate. Each source creates a spherical sound wave that propagates through a quiescent medium with constant speed of sound a. The source distribution is stationary with time. A number of fixed and scanning microphones are deployed. Scanning sensor m traverses on a plane through the source axis with speed V_m along a trajectory with local inclination angle β relative to the source line. Of interest here is the application of the DAS beamforming method to the continuous-scan paradigm.

B. Signal Division

For a scanning sensor, the recorded signal $p_m(t)$ is non-stationary in time due to the time-varying source-sensor distance and the spatial non-uniformity of the traversed acoustic field. Quasi-stationarity is sought by dividing the

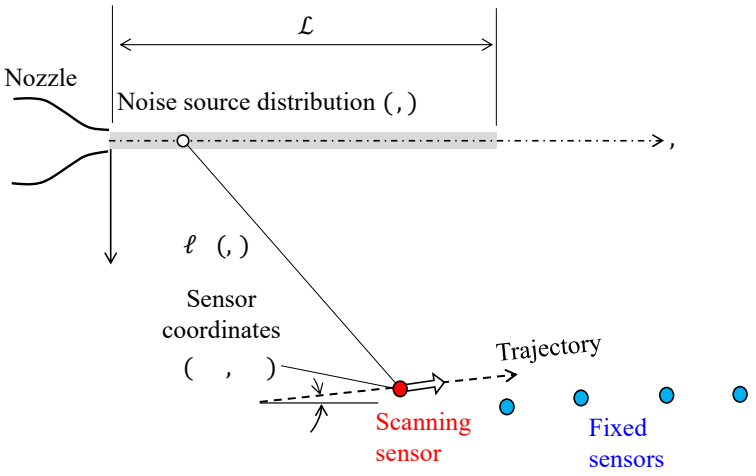

Fig. 1 Line source and sensor deployment.

signal into a number K of overlapping or non-overlapping blocks of duration T, as illustrated in Fig. 2. Correlations are then performed for each block k with center time t_k. Guidance for block division and associated signal processing can be found in Refs. [19, 20].

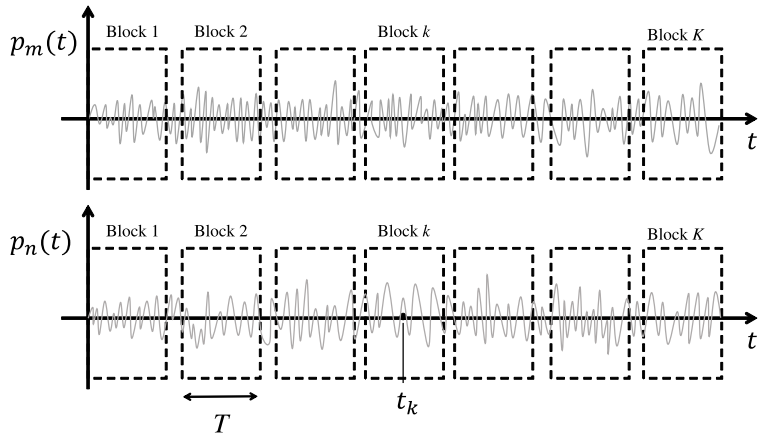

Fig. 2 Illustration of the division of the signal into K quasi-stationary blocks without block overlap.

Considering an array with M_f fixed and M_s scanning microphones, division of the signal into K blocks can be thought of as increasing the sensor count to $M_f + KM_s$. However, it is immediately obvious that not all of these sensors can be correlated. In particular, the signals of a given scanning sensor at different spatial positions (different blocks) are asynchronous and thus cannot be correlated. When considering the cross-spectral matrix (CSM) based on the sensor count $M_f + KM_s$, the matrix has missing entries, hence it is incomplete. This is illustrated in the example of Fig. 3a, where three microphones are fixed and one microphone is scanning. The signal of the scanning microphone is divided into six blocks. Treating the position of the scanning microphone as a “virtual" sensor, one is tempted to construct

a 9×9 cross-spectral matrix. Auto- and cross-correlations are possible between the fixed microphones, between the scanning and fixed microphones, and the scanning sensor with itself at a given block. However, correlations of the scanning sensor at different blocks are not possible. These are indicated by the blank entries in Fig. 3a.

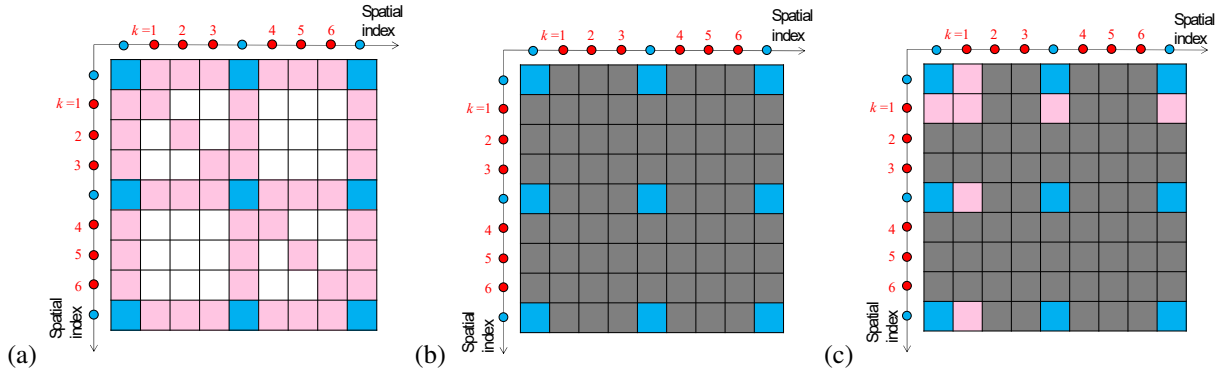

Fig. 3 (a) Cross-spectral matrix for an array with three fixed microphones and one scanning sensor whose output is divided into six blocks. The correlations involving fixed sensors only are highlighted in blue, while those involving fixed and scanning sensors are indicated in pink. Blank entries indicate missing elements. (b) Submatrix for block 0. (c) Submatrix for block 1.

Past beamforming studies using direct spectral estimation [19, 20] have also divided the signal into a number K of blocks and obtained a cross-spectral submatrix (CSSM) for each block k, with $k = 0$ encompassing the correlations between the fixed sensors only. This is illustrated in Figs. 3(b) and (c) for blocks $k = 0$ and $k = 1$, respectively, where the grayed regions indicate removal of rows and columns. These submatrices have repeated elements, comprising the correlations between fixed sensors, that must be excluded when combining their contributions. Figure 4 provides a more detailed example of submatrices obtained with two microphones scanning (sensors 1-2) and five being fixed (sensors 3 - 7). The contributions from the fixed and scanning sensors are highlighted in blue and pink, respectively. The elements marked in bold font are non-repeating and only those elements are used in constructing the array output. In this work, the approach illustrated in Fig. 4 is applied to the DAS method.

Block 0

3,3	**3,4**	**3,5**	**3,6**	**3,7**
4,3	**4,4**	**4,5**	**4,6**	**4,7**
5,3	**5,4**	**5,5**	**5,6**	**5,7**
6,3	**6,4**	**6,5**	**6,6**	**6,7**
7,3	**7,4**	**7,5**	**7,6**	**7,7**

Block 1

1,1	**1,2**	**1,3**	**1,4**	**1,5**	**1,6**	**1,7**
2,1	**2,2**	**2,3**	**2,4**	**2,5**	**2,6**	**2,7**
3,1	**3,2**	3,3	3,4	3,5	3,6	3,7
4,1	**4,2**	4,3	4,4	4,5	4,6	4,7
5,1	**5,2**	5,3	5,4	5,5	5,6	5,7
6,1	**6,2**	6,3	6,4	6,5	6,6	6,7
7,1	**7,2**	7,3	7,4	7,5	7,6	7,7

. . .

Block K

1,1	**1,2**	**1,3**	**1,4**	**1,5**	**1,6**	**1,7**
2,1	**2,2**	**2,3**	**2,4**	**2,5**	**2,6**	**2,7**
3,1	**3,2**	3,3	3,4	3,5	3,6	3,7
4,1	**4,2**	4,3	4,4	4,5	4,6	4,7
5,1	**5,2**	5,3	5,4	5,5	5,6	5,7
6,1	**6,2**	6,3	6,4	6,5	6,6	6,7
7,1	**7,2**	7,3	7,4	7,5	7,6	7,7

Fig. 4 Illustration of CSSMs for two scanning sensors (1-2) and three fixed sensors (3-7). Non-repeating elements are indicated in bold font.

There are advantages, however, to having a complete CSM. The simplicity of a single CSM obviates the logistical complexity of a large number of submatrices. Importantly, a complete CSM allows for the use of adaptive methods, advanced beamforming processes such as functional beamforming or orthogonal beamforming, and a straight-forward utilization of current deconvolution methods developed for fixed sensor arrays. It might be possible to extend deconvolution to the CSSM approach considering only the non-repeated elements of each CSSM. However, this was not studied in the present work. This work will consider two approaches for obtaining complete CSMs for the continuous-scan paradigm. The first is based on methodologies developed for non-synchronous array measurement and encompasses the fixed and scanning sensors. The second is based on partial fields decomposition and encompasses the scanning sensors only. In applying these methods, the elements of the incomplete CSM are sorted in space, as illustrated in Fig. 3 to facilitate the completion process.

C. Beamforming with Fixed Sensors (FS)

Beamforming with fixed sensors is briefly reviewed as it provides important background for the sections that follow. Considering $\mathcal{M}_f$ fixed sensors, the delay-and-sum signal in time domain is

$$s(\xi, t) = \sum_{m=1}^{\mathcal{M}_f} w_m \, p_m(t + \tau_m(\xi)) \tag{1}$$

where $p_m(t)$ is the signal measured by sensor m, w_m is a weight, and

$$\tau_m(\xi) = \frac{\ell_m(\xi)}{a} \tag{2}$$

is the source-sensor travel time.

The array output in frequency domain is proportional to the power spectral density of $s(\xi, t)$. It involves the CSM

$$\mathbf{G}(\omega) = G_{mn}(\omega) = \overline{P_m(\omega) P_n^*(\omega)} \tag{3}$$

where $P_m(\omega)$ and $P_n(\omega)$ are the Fourier transforms of $p_m(t)$ and $p_n(t)$, respectively, $*$ denotes the complex conjugate, and $\overline{()}$ represents the averaging in spectral estimation; and the steering vector

$$\mathbf{e}(\xi, \omega) = e_m(\xi, \omega) = w_m \exp[i\omega\tau_m(\xi)] \tag{4}$$

It can be readily derived that the normalized array output is

$$Y(\xi, \omega) = \frac{1}{\mathcal{M}_f^2} \, \mathbf{e}(\xi, \omega) \, \mathbf{G}(\omega) \, \mathbf{e}^H(\xi, \omega) \tag{5}$$

where H denotes the complex transpose.

Denoting the Fourier transform of the source $q(\xi, t)$ as $Q(\xi, \omega)$, for a spatially incoherent source

$$\overline{Q(\xi,\omega)Q^*(x,\omega)} = \Phi(x,\omega)\delta(x-\xi) \tag{6}$$

It is then straight-forward to show that the array output can be expressed as [3]

$$Y(\xi,\omega) = \int_{\mathcal{L}} \mathcal{S}(x,\xi,\omega)\,\Phi(x,\omega)\,dx \tag{7}$$

where

$$\mathcal{S}(x,\xi,\omega) = \sum_{m=1}^{\mathcal{M}_f}\sum_{n=1}^{\mathcal{M}_f} w_m w_n e^{i\omega[\tau_m(x)-\tau_m(\xi)]} e^{i\omega[\tau_n(\xi)-\tau_n(x)]} \tag{8}$$

is the point spread function (PSF), which represents the response of the array to a point source at location x. The array output therefore is the convolution between the source distribution $\Phi(x, \omega)$ and the PSF.

The dynamic range of the array can be improved by removing the diagonal terms of the CSM which contain the microphone self-noise contamination. However, diagonal removal can result in negative eigenvalues, associated with negative source auto-powers, which are unphysical and might impair advanced beamforming processes such as Functional Beamforming [33, 34]. An alternative approach to the diagonal removal method is the diagonal reconstruction method (DiRec) of Hald [35] or that of Dougherty [36]. The DiRec method can be understood as a semidefinite programming (SDP) problem, thus allowing the use of powerful convex optimization libraries such as CVX [37, 38]. No negative eigenvalues are obtained if using these methods. A comprehensive review on CSM denoising is found in Ref. [39].

D. Beamforming with Cross-Spectral Submatrices (CSSM)

The DAS method is extended to phased arrays containing fixed and continuously-scanning sensors, using the method of CSSM. Relations are first obtained on a per block basis, then the outputs of the blocks are assembled into an overall array output.

1. Array Output per Block

For a scanning sensor, the source-sensor travel time varies with time. Considering block k with center time t_k and duration T, subscript mk denotes the quantities associated with sensor m at $t = t_k$. Provided that T is sufficiently short, the source-sensor travel is approximated by the first-order Taylor expansion

$$\tau_m(\xi,t) \approx \tau_{mk}(\xi) + \alpha_{mk}(\xi)(t-t_k) \tag{9}$$

where

$$\alpha_{mk}(\xi) \;=\; \left.\frac{\partial \tau_m(\xi,t)}{\partial t}\right|_{t=t_k} \tag{10}$$

For the geometry of Fig. 1 it can be readily derived that

$$\alpha_{mk}(\xi) \;=\; \frac{V_{mk}}{a}\,\frac{(x_{mk}-\xi)\cos\beta - y_{mk}\sin\beta}{\ell_{mk}(\xi)} \tag{11}$$

where V_{mk} is the velocity of the scanning sensor and (x_{mk}, y_{mk}) are the sensor coordinates.

Considering $\mathcal{M}_f$ fixed and $\mathcal{M}_s$ scanning sensors, for block k the DAS signal in time domain follows Eq. 1 but with the above adjustment of the source-sensor time:

$$s_k(\xi,t) = \sum_{m=1}^{\mathcal{M}_f+\mathcal{M}_s} w_m p_{mk}[(1+\alpha_{mk}(\xi))t + \tau_{mk}(\xi)] \tag{12}$$

where $p_{mk}(t)$ is the pressure recorded by sensor m at block k and has a Fourier transform $P_{mk}(\omega)$. For simplicity time t is now referenced to the center time t_k. The Fourier transform of $s_k(\xi,t)$ is

$$\begin{aligned} S_k(\xi,\omega) &= \int_{-\infty}^{\infty} \sum_{m=1}^{\mathcal{M}_f+\mathcal{M}_s} w_{mk}\; p_{mk}[(1+\alpha_{mk}(\xi))t + \tau_{mk}(\xi)]\; e^{-i\omega t}\,dt \\ &= \sum_{m=1}^{\mathcal{M}_f+\mathcal{M}_s} \frac{w_{mk}}{1+\alpha_{mk}(\xi)}\, P_{mk}(\omega'_{mk}(\xi))\; e^{i\omega'_{mk}\tau_{mk}(\xi)} \end{aligned} \tag{13}$$

where $\omega'_{mk}(\xi)$ is the Doppler-shifted frequency

$$\omega'_{mk}(\xi) = \frac{\omega}{1+\alpha_{mk}(\xi)} \tag{14}$$

For low scan Mach number (i.e., $V_{mk}/a_\infty << 1$), the Fourier transform of the pressure signal $P_{mk}(\omega'_{mk})$ can be approximated as $P_{mk}(\omega)$ with little error. On defining the modified weights

$$W_{mk}(\xi) = \frac{w_m}{1+\alpha_{mk}(\xi)} \tag{15}$$

Eq. 13 becomes

$$S_k(\xi,\omega) = \sum_{m=1}^{\mathcal{M}_f+\mathcal{M}_s} W_{mk}(\xi)\; P_{mk}(\omega)\; e^{i\omega'_{mk}\tau_{mk}(\xi)} \tag{16}$$

The non-normalized array output for block k is $\overline{S_k(\xi,\omega)S_k^*(\xi,\omega)}$ and takes the form

$$Y_k(\xi,\omega) = \sum_{m=1}^{\mathcal{M}_f+\mathcal{M}_s} \sum_{n=1}^{\mathcal{M}_f+\mathcal{M}_s} W_{mk}(\xi)W_{nk}(\xi)\,\overline{P_{mk}(\omega)P_{nk}^*(\omega)}\; e^{i\omega'_{mk}(\xi)\tau_{mk}(\xi)}\; e^{-i\omega'_{nk}(\xi)\tau_{nk}(\xi)} \tag{17}$$

Defining the CSSM for block k as

$$\mathbf{G}_k(\omega) = G_{mn,k}(\omega) = \overline{P_{mk}(\omega)P_{nk}^*(\omega)} \tag{18}$$

with a size of $(\mathcal{M}_s + \mathcal{M}_f) \times (\mathcal{M}_s + \mathcal{M}_f)$, the array output for block k is

$$Y_k(\xi,\omega) = \mathbf{e}_k(\xi,\omega)\;\mathbf{G}_k(\omega)\;\mathbf{e}_k^H(\xi,\omega) \tag{19}$$

where

$$\mathbf{e}_k(\xi,\omega) \;=\; e_{mk}(\xi,\omega) \;=\; W_{mk}e^{i\omega'_{mk}(\xi)\tau_{mk}(\xi)} \tag{20}$$

is a modified steering vector with size $1 \times (\mathcal{M}_s + \mathcal{M}_f)$. For zero scan velocity, Eq. 20 reduces to Eq. 4 and Eq. 19 reduces to the conventional delay-and-sum beamforming expression of Eq. 5. The diagonal reconstruction methods mentioned earlier can still be applied to the array output of each block.

In calculating the auto- and cross-spectral densities of Eq. 18, care must be taken when handling non-stationary signals. As outlined in Ref. [19], the most serious manifestation of the non-stationarity is on the cross-correlations of sensors that have a relative velocity. Considering only one sensor scanning with speed V_m, this effect is suppressed when $V_m T << \lambda$, i.e., within each block the sensor travels a distance much smaller than the acoustic wavelength to be resolved. Changing the block size for each frequency would lead to a prohibitive computational cost for the array output. This motivates the implementation of a frequency-dependent Gaussian window within each block that is integrated with the spectral estimation and thus adds minimal cost to the computation. Denoting the window width δ, the suppression condition can be formulated as

$$V_m\delta \;=\; c_\lambda\lambda \tag{21}$$

where $c_\lambda << 1$. Connected with the implementation of the Gaussian window is the need for different Fast Fourier Transform sizes (N_{FFT}) across frequency ranges. The detailed procedures can be found in Ref. [19] and are followed here for the computation of the cross-spectral matrices for all the continuous-scan methods covered in this paper.

2. Overall Array Response

Equation 19 gives the array output for a given block k. In assembling the responses over all the blocks, only the non-repeating elements of the CSSMs (Eq. 18) are included to avoid averaging of repeated information. As illustrated in Fig. 4, the CSSM for the initial block, Block 0, comprises the signals of the fixed sensors only. Given

that only stationary signals are processed, the CSSM for Block 0 uses the entire duration of the signals. For the blocks $k = 1, 2, ..., K$ only the correlations with scanning sensors are used. It is easy to show that the number of non-repeating elements used to compute the array output is

$$J = (\mathcal{M}_f - \mathcal{M}_s)^2 + (K-1)\mathcal{M}_s(2\mathcal{M}_f - \mathcal{M}_s) \tag{22}$$

The array output for all the non-repeated elements of each CSSM is calculated as

$$\begin{aligned} Y(\xi,\omega) = \frac{1}{J}\Bigg\{ & \sum_{m=\mathcal{M}_s+1}^{\mathcal{M}_f+\mathcal{M}_s} \sum_{n=\mathcal{M}_s+1}^{\mathcal{M}_f+\mathcal{M}_s} w_m w_n \, G_{mn,0}(\omega) \, e^{i\omega\tau_m(\xi)} \, e^{-i\omega\tau_n(\xi)} + \\ & \sum_{k=1}^{K} \Bigg[\sum_{m=1}^{\mathcal{M}_s} \sum_{n=1}^{\mathcal{M}_f+\mathcal{M}_s} W_{mk}(\xi) W_{nk}(\xi) \, G_{mn,k}(\omega) \, e^{i\omega'_{mk}(\xi)\tau_{mk}(\xi)} \, e^{-i\omega'_{nk}(\xi)\tau_{nk}(\xi)} + \\ & \sum_{m=\mathcal{M}_s+1}^{\mathcal{M}_s+\mathcal{M}_f} \sum_{n=1}^{\mathcal{M}_s} W_{mk}(\xi) W_{nk}(\xi) \, G_{mn,k}(\omega) \, e^{i\omega'_{mk}(\xi)\tau_{mk}(\xi)} \, e^{-i\omega'_{nk}(\xi)\tau_{nk}(\xi)} \Bigg] \Bigg\} \end{aligned} \tag{23}$$

Referring to the illustration of Fig. 4, the first term on the right-hand side represents the contributions of Block 0 ($k = 0$, fixed sensors only); the second term reflects the first two rows for $k > 0$; and the third terms reflects the first two columns for $k > 0$, excluding the elements already accounted for. Because the first term involves only the fixed sensors, the frequency is not influenced by the Doppler shift. Equation 23 constitutes the extension of the delay-and-sum methodology to the continuous-scan paradigm using cross-spectral submatrices.

E. Beamforming using Cross-Spectral Matrix Completion (CSMC)

Research on noise source localization using a collection of non-synchronous microphone measurements has gained momentum [21–25]. An initial approach consisted in moving a prototype array sequentially. However, the phase relationships between the microphones of the array at two distinct sequential positions were lost, thus resulting in a penalization in the spatial resolution needed for beamforming applications. To overcome this problem, a strategy consisting of placing reference microphones near the source was later employed. Such microphones were used to recover the missing phase relationships between consecutive positions of the array by conditioned spectral analysis and principal component analysis [40] in a procedure similar to the partial fields decomposition presented in Section II.F. However, in order for the missing phase relationships to be sufficiently well resolved, a large number of reference sensors were usually needed to capture the number of distinct sources, resulting in a prohibitive cost for certain applications.

A novel approach of constructing the missing phase relationships of sequential microphone measurements was formulated in Refs. [41, 42]. The idea behind the methodology was the completion of the CSM obtained from non-synchronous microphone arrays (i.e., the estimation of the missing entries of an incomplete CSM). The approach has been successfully applied in the past to simulated sources and simple speaker sources [42], as well as some industrial

devices [43]. This section introduces a way to obtain a complete CSM that bears similarities to the spectral matrix reconstruction of Ref. [42]. The methodology is extended to the continuous-scan paradigm, thus reducing the total experimental time significantly [17] compared to sequential measurements. Other approaches were also explored but were unsuccessful. Specifically, a methodology similar to the array interpolation approach of Ref. [44] was tested; however, the spatial distribution of the noise sources at high frequency was relatively poor due to the phase unwrapping step not being perfectly linear with frequency.

The CSM completion method is usually stated as a matrix rank minimization problem (a low rank model) subject to some constraints. However, when dealing with signals produced by a large and unknown number of uncorrelated sources, as might be the case for jet noise, the process of estimating the rank of the completed matrix can be cumbersome without a priori information of the exact number of sources that produce the equivalent acoustic far-field signature. In addition, as discussed in Yu [42], the process of estimating the matrix rank poses a challenge when dealing with signals with moderate to high levels of noise in the measurements, as might be the case in wind tunnel beamforming applications. The rank minimization approach introduces a high degree of variability of the results as one must set a thresholding parameter, related to the most relevant eigenvalues of the completed CSM. Thus, the low rank model is usually reformulated as a weakly sparse eigenvalue spectrum problem. This enables the use of advanced semidefinite programming (SDP) algorithms and libraries used in convex optimization applications [37, 38]. Instead of imposing a reduced fixed rank, the completed CSM is of full rank and contains only a few dominant eigenvalues. The problem then results in minimizing the nuclear norm of the completed CSM subject to some constraints. Denoting the completed CSM as $\mathbf{G}_c$, its nuclear norm is

$$\|\mathbf{G}_c(\omega)\|_* = \sum_{j=1}^{\mathcal{M}_f+K\mathcal{M}_s} \lambda_j^2(\omega) \tag{24}$$

where λ_j are the eigenvalues. The completed CSM contains the contributions from fixed and scanning microphones, and has a size of $(\mathcal{M}_f + K\mathcal{M}_s) \times (\mathcal{M}_f + K\mathcal{M}_s)$ for each frequency resolved. The constraints needed to establish a unique and physical solution to the problem are described next.

The first restrictions imposed on the completed CSM are the Hermitian and semipositive definite conditions. That is

$$\mathbf{G}_c(\omega) \;=\; \mathbf{G}_c^H(\omega) \tag{25}$$

and

$$\mathbf{G}_c(\omega) \;\geq\; 0 \tag{26}$$

respectively. This ensures that there are no negative eigenvalues associated with negative auto-spectral densities. Next, a condition is imposed such that the completed CSM does not change the existing measured entries of the incomplete

CSM, denoted $\mathbf{G}_i$. This requirement can be relaxed and stated as

$$\|\mathcal{A}(\mathbf{G}_c(\omega)) - \mathbf{G}_i(\omega)\|_F \leq \epsilon_1 \tag{27}$$

where the $\mathcal{A}(\cdot)$ operator extracts the positions containing only the measured cross- and auto-spectral densities of the incomplete CSM, $\|\cdot\|_F$ is the Frobenius norm, and ϵ_1 is a thresholding error that relaxes the constraint.

A completed CSM can be calculated using the above requirements. However, the solution may not be unique or physical. Thus, a new constraint is included to obtain physical results. It ensures the smoothness of the acoustic far-field [45] by using a smoothing operator that encodes the positions of the microphones, fixed and scanning (i.e. the center of the blocks). The operator acts as a filter on the completed CSM, preventing significant variations between the auto- and cross-spectral densities of microphone pairs that are very close. The filter is denoted by $\mathbf{\Psi}$ and is constructed using a dimension-reduced Fourier spatial basis

$$\mathbf{\Theta} = \exp\left[i(\kappa_x \mathbf{x} + \kappa_y \mathbf{y})\right] \tag{28}$$

where $\mathbf{x}$ and $\mathbf{y}$ are the vectors of the x and y coordinates of the fixed sensors and center coordinates of the blocks, and (κ_x, κ_y) are spatial wavenumbers. Following the guidance of Yu *et al.* [42], the wavenumbers are discretized as $\kappa_x^n = n\Delta\kappa_x$, with $n = -N, ..., N$, and $\kappa_y^m = m\Delta\kappa_y$ and $m = -M, ..., M$. The expressions for κ_y will be obviated in the analysis that follows given their similarity to those obtained for k_x. The maximum spatial frequency is $\kappa_{x,\max} = N\Delta\kappa_x = \frac{\pi}{\Delta x}$. The spatial frequency can be related to the array aperture as $\Delta\kappa_x = \frac{2\pi}{L_x}$, where L_x is the aperture in the x direction, and similarly for M. Thus, the integer N is given by $N = \frac{\pi}{\Delta x \Delta\kappa_x}$, and similarly for M. Here, we assume that the acoustic waves will not change significantly within the small Δz offset between the fixed and scanning microphones (see Section III.B); hence we have not included the third dimension in our formulation. However, the methodology can be extended for sensors with greater Δz offsets. The choice of the above spatial basis is valid as long as the far-field correlation length ℓ_c is larger than the distance between neighboring microphones or block centers of the array. A general rule to determine the minimum resolution of the dimension-reduced basis is $\Delta x, \Delta y \geq \min(\ell_c, 2d_c)$, where d_c represents the distance between two contiguous microphones or block centers. In this study, we used $\Delta x = \Delta y \approx 2d_c$.

Then, the smoothing filter is constructed as

$$\mathbf{\Psi} = \mathbf{\Theta}\mathbf{\Theta}^{\dagger} \tag{29}$$

where $\mathbf{\Theta}^{\dagger}$ is the pseudo-inverse, which is found using the Moore-Penrose method. The Moore-Penrose inverse is

defined as $\mathbf{\Theta}^{\dagger} = \mathbf{V}\mathbf{\Sigma}^{-1}\mathbf{U}^{\mathbf{H}}$, where the rectangular diagonal matrix $\mathbf{\Sigma}^{-1}$ is

$$\mathbf{\Sigma}^{-1} = \begin{pmatrix} \sigma_{11}^{-1} & 0 & \cdots & 0 \\ 0 & \sigma_{22}^{-1} & \cdots & 0 \\ \vdots & \vdots & \ddots & \vdots \\ 0 & 0 & \cdots & \sigma_{2N\times 2M}^{-1} \end{pmatrix} \tag{30}$$

and contains non-negative numbers only; $\mathbf{\Theta} = \mathbf{U}\mathbf{\Sigma}\mathbf{V}^{\mathbf{H}}$ is the singular value decomposition of the matrix, where $\mathbf{V}$ and $\mathbf{U}$ are the singular value vector matrices; and $\mathbf{\Sigma}$ is a rectangular diagonal matrix containing the singular values. Note that M and N do not necessarily need to be equal, as they depend on the discretization used to obtain the reduced-dimension spatial basis. Obviously, the entries of the CSM must not be significantly changed as a consequence of the filtering, a requirement that is expressed as

$$\|\mathbf{\Psi}\mathbf{G}_c(\omega)\mathbf{\Psi}^{\mathbf{H}} - \mathbf{G}_c(\omega)\|_F \leq \epsilon_2 \tag{31}$$

where ϵ_2 is a thresholding error. Having introduced all the required variables, the problem of CSM completion for continuous-scan phased arrays is formulated as

$$\begin{aligned} \text{minimize} \quad & \|\mathbf{G}_c(\omega)\|_* \\ \text{subject to} \quad & \|\mathcal{A}(\mathbf{G}_c(\omega)) - \mathbf{G}_i(\omega)\|_F \leq \epsilon_1 \\ & \|\mathbf{\Psi}\mathbf{G}_c(\omega)\mathbf{\Psi}^{\mathbf{H}} - \mathbf{G}_c(\omega)\|_F \leq \epsilon_2 \\ & \mathbf{G}_c(\omega) = \mathbf{G}_c^H(\omega) \succeq 0 \end{aligned} \tag{32}$$

The above methodology has been successfully applied to block-Hermitian matrix completion problems in past beamforming studies [21–23, 42, 43, 45]. However, a key difference is that the incomplete CSM $\mathbf{G}_i$ obtained in the context of the continuous-scan paradigm is not in general block-Hermitian. The completed CSM is obtained, as per Eq. 32, using the Fast Iterative Shrinkage Thresholding Algorithm (FISTA) approach of Ref. [43].

The completed CSM is steered to location ξ within the region of interest to compute the array output as

$$Y(\xi,\omega) \;=\; \frac{1}{(\mathcal{M}_f + K\mathcal{M}_s)^2}\, \mathbf{e}(\xi,\omega)\, \mathbf{G}_c(\omega)\, \mathbf{e}^H(\xi,\omega) \tag{33}$$

Here, the steering vectors are of size $1 \times \left(\mathcal{M}_f + K\mathcal{M}_s\right)$. It is noted that diagonal removal or reconstruction algorithms can be used with the above approach, requiring appropriate adjustment to the denominator. The steering vector used in Eq. 33 has components associated with both fixed and continuously-scanning sensors. As such, Eq. 4 should be used for fixed sensors while Eq. 20 should be used for the components involving scanning sensors.

A cautionary comment is noted with regards to the errors associated with the estimation of the missing entries of the CSM, known as Matrix Completion Errors (MCE), and defined as

$$\mathrm{MCE}(\omega) = \frac{\|\mathbf{G}_{\mathrm{real}}(\omega) - \mathbf{G}_c(\omega)\|_F}{\|\mathbf{G}_{\mathrm{real}}(\omega)\|_F} \tag{34}$$

where $\mathbf{G}_{\mathrm{real}}$ is the real CSM. Past experimental results [43] have measured the performance of the matrix completion error in conjunction with the FISTA algorithm. It is found that the MCE is usually below 0.1 when the signal-to-noise ratio is below 10 dB using exclusively sequential measurements (i.e. without the use of any reference sensors). The MCE improves when utilizing reference sensors and appears independent of the number of references used. As such, FISTA is identified as a robust method of minimizing Eq. 32 when the number of uncorrelated acoustic sources is unknown a priori. No specific trends of the MCE as a function of frequency are noted, as it does not monotonically increase or decrease [42]. The matrix completion problem posed in the present work might be considered as an extension of the FISTA matrix reconstruction problem of Ref. [43], where the reference sensors are the fixed microphones and the sequential measurements are given by the scanning microphone.

F. Beamforming using Partial Fields Decomposition (PFD)

An alternative way to construct a cross-spectral matrix involves the method of partial fields decomposition (PFD). A similar approach has been used before by Shah *et al.* [46, 47], and has been successfully applied in the beamforming of fan and jet noise sources [46, 48] and near-field acoustic holography [11, 49, 50]. The method can be considered an extension of the start-and-stop method [11, 49, 50], which relied on having an array of *reference* (fixed) sensors that were measuring continuously while a small subset of the array was scanning over a number of patches sequentially. In this study, the microphone is continuously scanning, and the signal is non-stationary, requiring advanced spectral estimation techniques and division of the signal into smaller and quasi-stationary blocks, as discussed in Section III.B.

In contrast with the CSM completion approach of the previous section, here the cross-spectral matrix is based on the scanning microphones only. The fixed microphones are used for phase-referencing.. A brief summary of the process is provided. First, a reference CSM is constructed using the entire duration of the signal of the fixed sensors only:

$$\mathbf{G}_{ff,T}(\omega) = G_{f_m f_n,T}(\omega) \;=\; \overline{P_{f_m,T}(\omega) P^*_{f_n,T}(\omega)} \tag{35}$$

Subscript ff indicates correlations between fixed sensor only and subscript T indicates the entire duration of the signal). The reference CSM has a singular value decomposition

$$\mathbf{G}_{ff,T} \;=\; \mathbf{U}_{ff,T} \mathbf{\Sigma}_{ff,T} \mathbf{V}^H_{ff,T} \tag{36}$$

The pressure signals from all sensors (fixed and scanning) are then divided into a number K of overlapping or non-overlapping blocks, similarly to the previously-described approaches. A transfer function matrix between the reference microphones and the continuously-scanning sensors is constructed for every block as

$$\mathbf{H}_{fs,k} = \left(\mathbf{G}_{ff,k}\right)^{-1}\mathbf{G}_{fs,k} \tag{37}$$

where $\mathbf{H}_{fs,k}$ represents the transfer function matrix for block k. The term $\mathbf{G}_{ff,k}$ is the CSM calculated utilizing the fixed sensors only for block k, obtained using

$$\mathbf{G}_{ff,k}(\omega) = G_{f_m f_n,k}(\omega) \;=\; \overline{P_{f_m,k}(\omega)P^*_{f_n,k}(\omega)} \tag{38}$$

and $\mathbf{G}_{fs,k}$ is the CSM obtained utilizing the fixed sensors and the scanning microphones, which is computed as

$$\mathbf{G}_{fs,k}(\omega) = G_{f_m s_n,k}(\omega) \;=\; \overline{P_{f_m,k}(\omega)P^*_{s_n,k}(\omega)} \tag{39}$$

Note that while $\mathbf{G}_{ff,k}$ is always a square Hermitian matrix, $\mathbf{G}_{fs,k}$ does not necessarily need to be square. The frequency-dependent window is applied in the cross-spectral density estimation of $\mathbf{G}_{fs,k}$ in a similar way as in Ref. [19], as outlined in the preceding sections. Typically, the matrix $\mathbf{G}_{ff,k}$ does not have an inverse. It is a standard procedure to use the Moore-Penrose generalized inverse for the matrix such that

$$\left(\mathbf{G}_{ff,k}\right)^{-1} = \left(\mathbf{G}_{ff,k}\right)^{\dagger} = \mathbf{V}_{ff,k}\mathbf{\Sigma}^{-1}_{ff,k}\mathbf{U}^H_{ff,k} \tag{40}$$

where

$$\mathbf{G}_{ff,k} = \mathbf{U}_{ff,k}\mathbf{\Sigma}_{ff,k}\mathbf{V}^H_{ff,k} \tag{41}$$

is the singular value decomposition of the matrix, where all the above relationships are valid for each frequency ω analyzed.

The partial fields for block k, calculated at the geometric center of the block, are given by

$$\mathbf{\Pi}_k = \mathbf{H}^H_{fs,k}\mathbf{U}_{ff,T}\mathbf{\Sigma}^{1/2}_{ff,T} \tag{42}$$

The CSM obtained via PFD, denoted $\mathbf{G}_{\mathrm{PF}}$, is then constructed by "sewing" the partial fields together, as outlined in Ref. [46]:

$$\mathbf{G}_{\mathrm{PF}} \;=\; \mathbf{\Pi}^H_i\mathbf{\Pi}_j \;\;,\;\; i,j = 1,\ldots,K \tag{43}$$

It has a size of $K\mathcal{M}_s \times K\mathcal{M}_s$. The noise source distribution can be obtained by steering the CSM using the delay-and-sum algorithm as

$$Y(\xi,\omega) = \frac{1}{(K\mathcal{M}_s)^2}\, \mathbf{e}_{\mathrm{PF}}(\xi,\omega)\, \mathbf{G}_{\mathrm{PF}}(\omega)\ \ \mathbf{e}_{\mathrm{PF}}^{H}(\xi,\omega) \tag{44}$$

where the steering vector is assembled as

$$\mathbf{e}_{\mathrm{PF}} \ = \ W_{mk} \exp[i\omega'_{mk}\tau_{mk}]\ , \ \ m = 1,\ldots,\mathcal{M}_s\ ,\ k = 1,\ldots,K \tag{45}$$

and has size $1 \times K\mathcal{M}_s$.

Care must be taken when interpreting the results obtained with PFD. The PFD technique decomposes the measured acoustic field into a number of mutually orthogonal and coherent partial fields (Eq. 42). The partial fields are then "sewed" together to construct a CSM based on the locations of the scanning sensor. The CSM can be used consistently with the uncorrelated line source model of Fig. 1. The quality of the CSM depends on whether the number of partial fields utilized for its construction is sufficient to adequately represent the acoustic field emitted by the source. This number depends on the number of fixed microphones used to construct the reference CSM. For the supersonic jet noise source of this work, the ranked singular values of the reference CSM are well separated for frequencies up to about 50 kHz, as shown in Fig. 13. Importantly, the tonal components for $f \leq 50$ kHz are adequately captured by the leading partial field. Application of this method for high frequency would require a larger number of partial fields, hence a larger number of fixed reference sensors [50].

G. Deconvolution Methods

For phased arrays that include scanning sensors, the convolution formula of Eq. 7 still holds with the modified PSF

$$\mathcal{S}(x,\xi,\omega) = \sum_{m=1}^{\mathcal{M}}\sum_{n=1}^{\mathcal{M}} W_m(\xi)W_n(\xi)W_m(x)W_n(x) e^{i\omega'[\tau_m(x_0)-\tau_m(\xi)]} e^{i\omega'[\tau_n(\xi)-\tau_n(x_0)]} \tag{46}$$

where $\mathcal{M}$ represents the number of sensor locations ($\mathcal{M}_f$ when using fixed sensors only; $\mathcal{M}_f + K\mathcal{M}_s$ for CSMC; and $K\mathcal{M}_s$ for PFD). The modified weights W are given by Eq. 15 and the Doppler-shifted frequency ω' is given by Eq. 14. Careful bookkeeping of the terms in Eq. 46 is required to apply these equations correctly. Upon discretization the integral of Eq. 7 becomes a linear system of equations whose inversion can be addressed by a number of methods.

Several deconvolution approaches have been proposed to improve the spatial resolution of the image and reject the sidelobes that are inherent in the PSF. This study explored three of such methods: DAMAS [4], Richardson-Lucy algorithm (RL) [3, 51–53] and CLEAN-SC [5]. These schemes were not applied with the CSSM method. In all of the above approaches, the sources are assumed to be uncorrelated. DAMAS inverts Eq. 7 using the Gauss-Seidel method. In the RL approach the PSF and source distribution are treated as conditional and independent probabilities,

respectively, and inversion uses Bayes' theorem. CLEAN-SC is based on the fact that the sidelobes are coherent with the main lobe; it removes, the sidelobe contributions iteratively to refine the noise source distribution. In doing so, the contributions from the peak sources are removed from the completed CSM, thus forming a degraded version of the matrix. The process stops when the CSM is sufficiently degraded. CLEAN-SC may have difficulty localizing a large number of spatially incoherent sources, tending to merge closely-spaced sources into a single source of higher intensity [54]. The process can be improved using a high-resolution version of CLEAN-SC [55].

For the DAMAS and RL methods the convergence error at a given frequency is defined as

$$\epsilon_d(\omega) \;=\; \frac{1}{\mathcal{L}\, Y_{\max}} \int_{\mathcal{L}} \left| Y(\xi,\omega) - \int_{\mathcal{L}} \mathcal{S}(x,\xi,\omega)\; \Phi(x,\omega) dx \right| \; d\xi$$

where $Y_{\max}$ is the maximum value of the array output at a given frequency. Convergence required $\epsilon_d(\omega) \leq 0.1$. The stopping criterion for the CLEAN-SC method was

$$\|\mathbf{G}_{\text{degraded}}\|_F > \|\mathbf{G}\|_F$$

III. Experimental Setup

A. Phased Microphone Array

Noise measurements were conducted in the UCI Aeroacoustics Facility depicted in Fig. 5. The room is covered with anechoic foam wedges having a half-wedge angle of 23° and depth of 152 mm. The reverberation time is 0.5 s and the approximate cut-off frequency is 560 Hz [56]. The microphone array comprises twenty-four 1/8-inch condenser microphones (Brüel and Kjaer, Model 4138) with frequency response up to 120 kHz. The microphones are connected, in groups of four, to six conditioning amplifiers (Brüel and Kjaer, Model 2690-A-0S4). The outputs of the amplifiers are sampled simultaneously, at 250 kHz per channel, by three 8-channel multi-function data acquisition boards (National Instruments PCI-6143) installed in a computer with an Intel i7-7700K quad-core processor. National Instruments Labview software provides the interface for signal acquisition and filtering, as well as control of the experiment. The microphone signals were conditioned with a high-pass filter set at 350 Hz to remove any spurious noise. Temperature and humidity inside the chamber were recorded to enable the calculation of the effects of atmospheric absorption.

Far-field noise measurements were conducted with the microphones mounted on a linear inclined holder with inclination angle $\beta = 11.3°$ with respect to the jet axis. The beamforming results presented here utilized thirteen fixed microphones ($\mathcal{M}_f = 13$) in combination with one scanning microphone ($\mathcal{M}_s = 1$), as shown in Fig. 6. This arrangement covered the polar sector $55° \leq \theta \leq 101°$, which is relevant to the screech emission of the jet flow considered here. The scanning microphone was mounted on a linear traverse consisting of a belt drive (Igus ZLW-0630) powered by a servo motor (ClearPath MCPV). The trajectory of the scanning microphone was parallel to the fixed microphone line, with a

lateral offset $\Delta z = -6$ mm. The mean distance of the sensors to the source origin $(0, 0, 0)$ was $R = 1.02$ m. The array linear aperture was $L = 0.85$ m for the fixed sensors only and $L = 0.90$ m when the scanning sensor was added.

The position of the scanning microphone was determined from the encoder signal of the motor (ClearPath MCPV) powering the traverse and verified by a laser displacement sensor (SICK OD1000). The servo was programmed to rotate at fixed revolutions per minute with a velocity ramp-up and ramp-down to prevent damage to the scanning microphone. The steady-state speed was of 75.94 mm/s, with a stroke length of 900 mm. A total of 3×10^6 samples were acquired for each channel, corresponding to an acquisition time of 12 s. Further details on the scanning microphone setup can be found in Ref. [19].

Sound Pressure Level (SPL) spectra were computed from the microphone signals using $N_{\text{FFT}} = 4096$, giving a frequency resolution of 61 Hz. The SPL spectra were corrected for actuator response, microphone free-field response, and atmospheric absorption. They are referenced to a constant radius of 0.305 m from the nozzle exit. In the beamforming procedures, the signals of the 14 microphones were divided into a total of $K = 352$ blocks following the signal division guidance of Ref. [20]. The block schedule utilized a block size of 32768 samples, corresponding to 0.13 s and a traversed distance of 10 mm. The block overlap was approximately 50%. The window parameter of Eq. 21 was $c_\lambda = 0.2$. The frequency ranges 0 - 55 kHz, 55-85 kHz, and 85-120 kHz were processed with $N_{\text{FFT}} = 1024$, 512, and 256, respectively, following the guidelines of Ref. [19]. The region of interest along the source axis was set to -0.3 m $\leq x \leq$ 0.6 m. For the main part of the investigation it was divided into 350 increments with resolution $\Delta x =$ 2.7 m. Investigation of a synthetic source with very fine features required a much finer resolution of 0.4 mm.

The guidance from Ref. [4] was used for the deconvolution approaches to avoid spatial aliasing problems. Specifically, the ratio $\Delta x / B_{\text{-3 dB}}$ was kept approximately constant and equal to 0.2, where $B_{\text{-3 dB}}$ is the main lobe beam width (-3 dB cutoff beam width) taken at $x = 0$ m. This led to a frequency-dependent number of divisions of the region of interest, rapidly increasing with frequency. To limit the computational cost of the inversion process, the maximum number of grid points at high frequency was capped at 350, thus yielding a finest spatial resolution of $\Delta x = 2.7$ mm.

B. Noise Sources

This study examined two noise sources: a synthetic source distribution and a supersonic underexpanded jet. The synthetic source was used as a benchmark to quantify the errors in the source localization and source strength for the beamforming methods investigated. It comprised 18 uncorrelated monopoles with frequency range 1 kHz to 90 kHz, as shown in Fig. 7. The amplitude of the distribution was constant throughout. The monopoles occupied the region $x \in [0, 0.2]$ m and were equally spaced at 0.0106 m. This spacing corresponds, approximately, to the size of the main beamwidth at 36 kHz for FS, and at 32 kHz for the continuous-scan methods. The pressure field caused by the synthetic source was propagated to the locations of the fixed and scanning microphones, shown in Fig. 6. The position of the scanning microphone was determined from the encoder signal of the motor used in the experiments. A

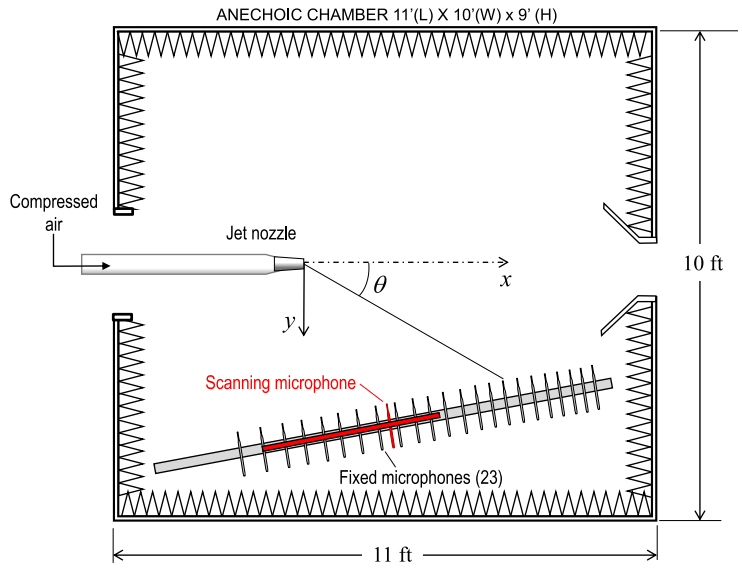

Fig. 5 Diagram of the UCI anechoic chamber. The scanning microphone is indicated in red.

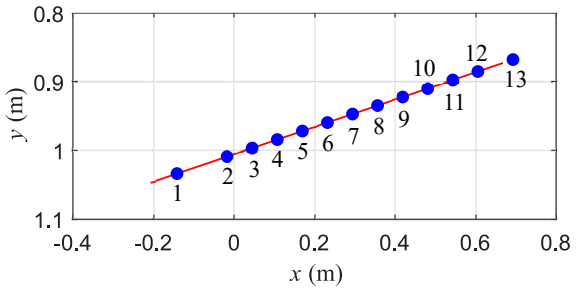

Fig. 6 Coordinates of fixed microphone coordinates (blue) and trajectory of scanning microphone (red).

sampling frequency of 250 kHz and 12 seconds of recording time were used, consistently with the actual experimental conditions.

The supersonic jet issued from a convergent round nozzle with exit diameter $D = 14.2$ mm and lip thickness of 0.4 mm. The nozzle coordinates are plotted in Fig. 8. The nozzle was supplied by air at room temperature and total pressure of $p_0 = 297$ kPa. This resulted in a fully-expanded jet Mach number $M_j = 1.34$ and fully-expanded velocity $U_j = 397$ m/s. At these conditions the jet emits strong screech tones that correspond to the lateral mode of oscillation, called mode B. This source was selected due to the richness of the far-field acoustic components, including the turbulence mixing noise, broadband shock-associated noise and screech tones. Structures upstream of the nozzle were covered with anechoic foam to minimize any reflections towards the nozzle. The Reynolds number based on nozzle exit diameter was 6.5×10^5. During each experimental run, the total pressure was held to within 1% of its target value.

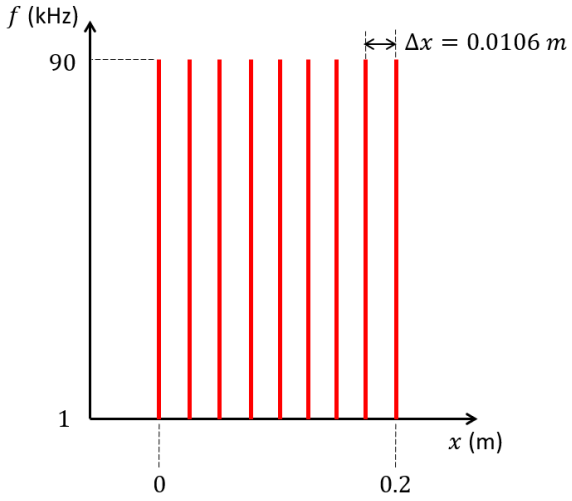

Fig. 7 Distribution of synthetic noise source.

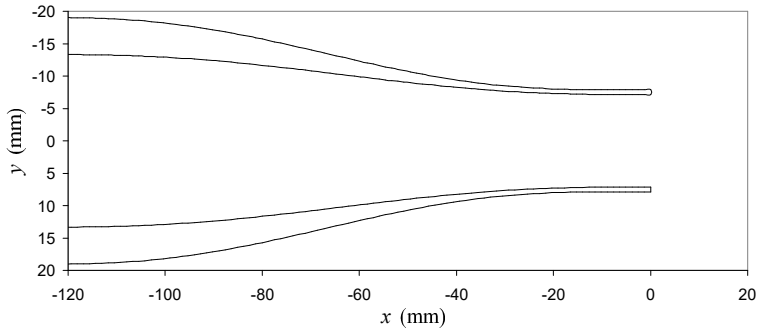

Fig. 8 Nozzle coordinates on symmetry plane.

IV. Results

Results are presented relating to the delay-and-sum array output obtained by the methods of Section II. Results obtained using fixed sensors only will be denoted by FS; those obtained using the continuous-scan paradigm will be denoted CSSM, CSMC, and PFD for the cross-spectral submatrix, cross-spectral matrix completion, and partial fields decomposition methods, respectively. The array output Y has natural units of Pa^2/Hz and will be presented in decibel scale as dB/Hz. Accordingly, the noise source distribution obtained after deconvolution has units of dB/(m Hz).

A. Array Pattern

The array point spread function (Eq. 46) affects the spatial resolution and fidelity of the beamforming. The PSF typically contains a main lobe that can detect the true source location and sidelobes that can severely distort the array output and create images of artificial sources. Past research has been conducted on optimizing the array geometry to improve the spatial resolution of the beamformed images [1, 57]. However, the sidelobes can only be suppressed to a

certain extent. With regards to the main lobe beam width, it scales approximately as $B_{-3\text{dB}} \approx CR/(\lambda L)$ where C is an experimentally-determined dimensionless constant [4].

Figure 9 displays the PSF for a point source at $x = 0$ m, normalized for each frequency. The figure demonstrates the significant sidelobe suppression enabled when using the continuous-scan techniques compared to utilizing an array containing only fixed sensors. Regarding the main lobe width, the empirical constant in the above expression drops from $C \approx 0.90$ for FS to $C \approx 0.79$ for the continuous-scan methods. Thus, in addition to the suppression of the sidelobes, an 18% improvement in the spatial resolution of the main lobe is attained by including a scanning microphone.

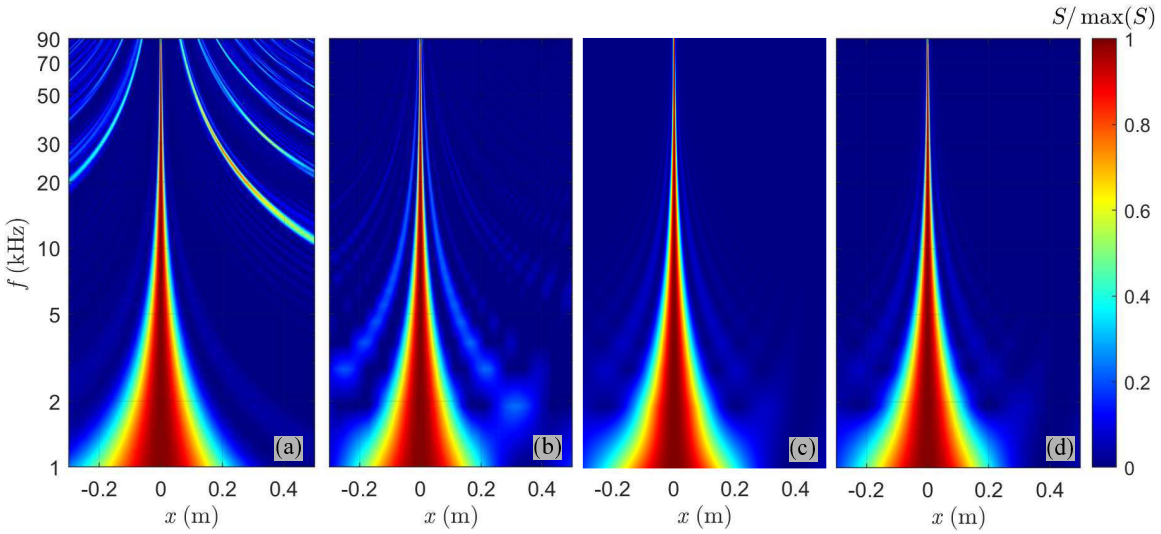

Fig. 9 Normalized point spread function $S(x, 0, \omega)/S_{max}(0, \omega)$ for: (a) FS; (b) CSSM; (c) CSMC; (d) PFD.

B. Synthetic Noise Sources

Contour plots of the array output Y for the synthetic source of Fig. **??**, calculated using FS, PFD, and PFD deconvolved using DAMAS, are shown in Fig. 10. The results for CSSM and CSMC are similar to those for PFD and therefore are omitted. The distributions are normalized by their peak values for each frequency to aid the interpretation of the results. It is evident that FS fails at detecting the source locations. On the other hand, PFD (before and after deconvolution) provides sharp images of the noise sources for $f >$ 50 kHz. The beamforming of the noise sources at lower frequencies is affected by the size of the main lobe beamwidth and results in a poor source separation, as seen in the figure.

Figure 11 plots the array output distributions of Fig. 10 at $f = 60$ kHz. FS suffers from strong sidelobes and produces a pattern that bears little resemblance to the actual source distribution. The maximum values of PFD shows distinct peaks associated with each of the 18 source locations. Deconvolution narrows the beamwidth and thus sharpens those peaks significantly.

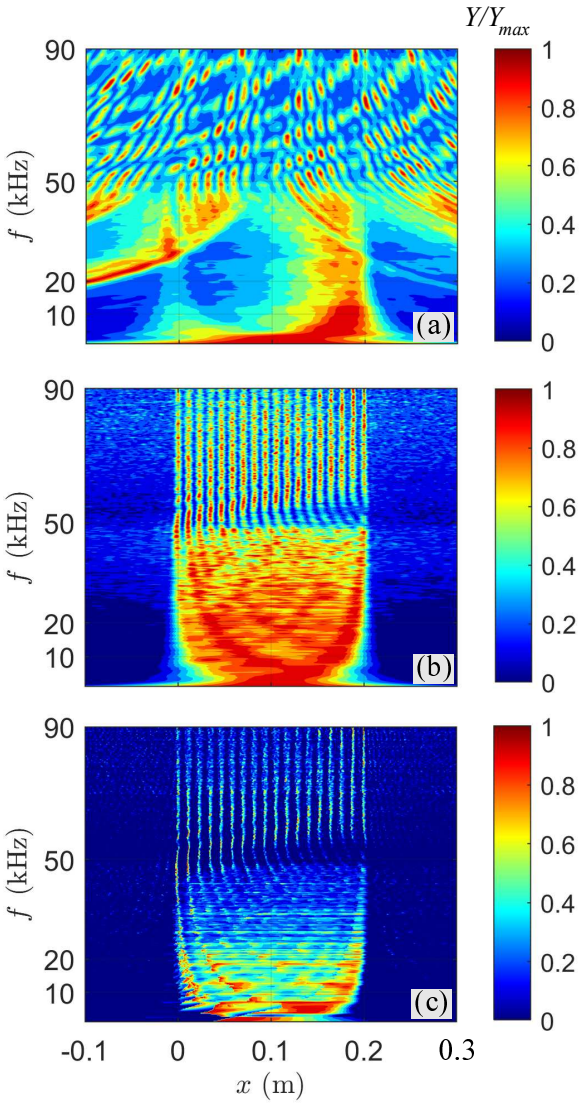

Fig. 10 Maps of array output for the synthetic noise source. (a) FS; (b) PFD; (c) PFD followed by DAMAS deconvolution. Maps are normalized by the local maximum.

The synthetic-source results allow quantification of the errors associated with each of the imaging techniques. For a given frequency, the source localization error is defined as

$$\epsilon_x = \sqrt{\frac{1}{N}\sum_{i=1}^{N}(\widetilde{X}_i - X_i)^2}$$

where X_i is the true position of source i, $\widetilde{X}_i$ is the location of the peak of source i as determined by beamforming, and $N = 18$ is the total number of sources. For FS, this error could not be quantified at any frequency because of the confusion between main lobe and sidelobes. It suffices to say that the error of FS is unacceptably high for imaging sources with fine features. For the continuous-scan methods, the error location can be quantified for $f \geq 50$ kHz. At

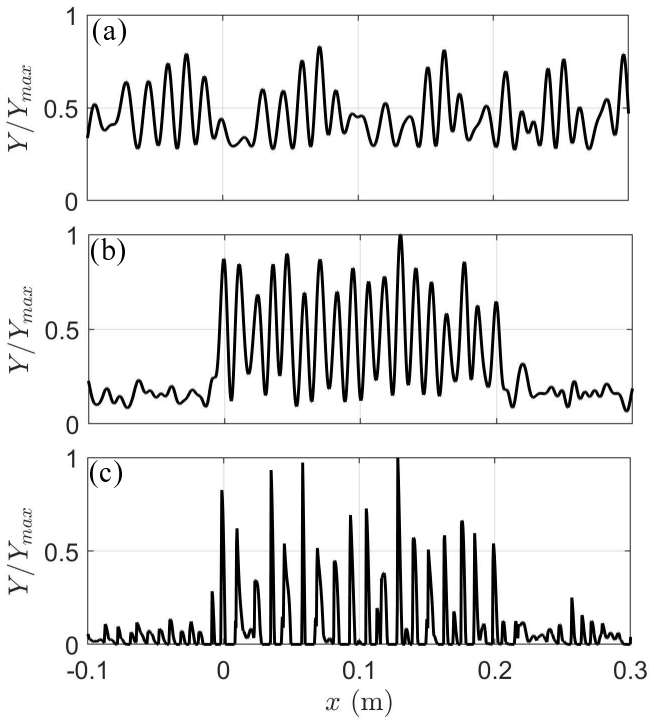

Fig. 11 Axial distributions of array outputs for the synthetic noise source at $f = 60$ kHz. (a) FS; (b) PFD; (c) PFD followed by DAMAS deconvolution. Outputs are normalized by the local maximum.

lower frequencies, the beamwidth is too large to resolve the finely-spaced sources. At $f = 60$ kHz, the location errors for CSSM, CSMC, and PFD were 0.91 mm, 0.67 mm, and 0.78 mm, respectively. PFD after deconvolution yielded an error of 0.63 mm. These errors are on the order of $\sim 5\%$ or less of the diameter of the nozzle used in the jet experiment. Results at higher frequencies are similar.

The source strength error measures the deviation of the beamformed output, at the imaged source location, from a uniform distribution consistent with the definition of the synthetic source. The error is relative to the mean distribution, in decibels,

$$\overline{Y}_{\mathrm{dB}} \;=\; \frac{1}{N}\sum_{i=1}^{N} 10\log_{10} Y(\widetilde{X}_i)$$

and is defined as

$$\epsilon_s = \sqrt{\frac{1}{N}\sum_{i=1}^{N}\left[10\log_{10} Y(\widetilde{X}_i) \;-\; \overline{Y}_{\mathrm{dB}}\right]^2}$$

For FS, the strength error could not be evaluated due to the ambiguity in source location. From Fig. 11 is is evident that FS fails to even capture the extent of the source region. For the continuous-scan methods at f=60 kHz, the strength errors were: 0.91 dB, 1.02 dB, and 0.95 dB for CSSM, CSMC, and PFD, respectively. DAMAS deconvolution of the PFD output yielded a strength error of 1.05 dB. Thus, for all the continuous-scan methods, the departure from

uniformity was approximately 1 dB. The above location and strength errors indicate the potential for continuous-scan approaches to resolve noise sources with fine features, as is the case of the supersonic jet of this study.

C. Jet Noise Source

This section presents sound pressure level (SPL) spectra and phased-array results for the supersonic underexpanded jet. SPL spectra are based on the full record of the signals opf the fixed microphones (12 s). They are plotted for several polar angles at which one encounters a richness of tones. In the presentation of the results the notation $X^{(n)}$ is used to designate a screech tone, where X is the mode and n is the harmonic. The mode notation of Ref. [58] is followed, with mode B denoting a lateral oscillation. Figure 12 displays the lossless SPL spectra for the isolated jet. Tones $B^{(1)}$, $B^{(2)}$, $B^{(3)}$ and $B^{(4)}$ appear prominently. Their directivity is not uniform, hence their levels vary depending on the polar station [59, 60]. The frequency of tone $B^{(1)}$ is approximately 9200 Hz.

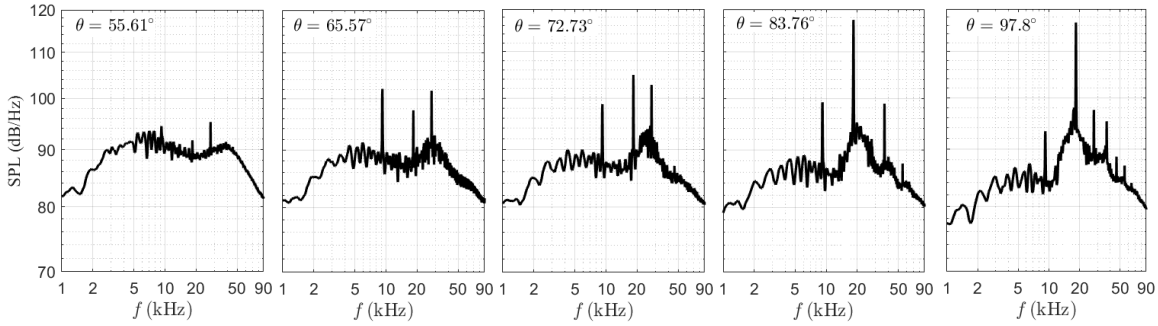

Fig. 12 SPL spectra for the underexpanded jet at various polar angles.

Some aspects of the PFD method are discussed before presenting the beamforming maps. Figure 13 shows the singular values of the diagonal of $\mathbf{\Sigma}_{ff,T}$, calculated using Eq. 36. The size of the $\mathbf{\Sigma}_{ff,T}$ matrix is of 13×13 and only the odd-numbered entries of the diagonal are displayed in the figure $(1, 3, 5, \ldots, 13)$. There is a relatively good separation (at least one order of magnitude) between the largest and the smallest singular values for frequencies up to 50 kHz, suggesting that the majority of the energy for such frequency range can be described utilizing a small number of partial fields. The screech tone and its four harmonics are well represented using one to three distinct orthogonal partial fields. Above this frequency the separation declines considerably and some degradation in the CSM ($\mathbf{G}_{\mathrm{PF}}$) is expected given the number of partial fields obtained might be less than the required to fully characterize the acoustic field emitted by the source, thus lowering the quality of the array output.

The accuracy of the CSMC and PFD techniques in generating a complete CSM is evaluated by examining the coherence along the array line of Fig. 6. Figure 14 plots the real part of the complex coherence versus polar angle for tones $B^{(1)}$ and $B^{(2)}$ between a reference sensor, marked with vertical blue line, and the scanning microphone. The black lines plot the coherence using an actual (fixed) microphone as the reference sensor. In the application the CSMC

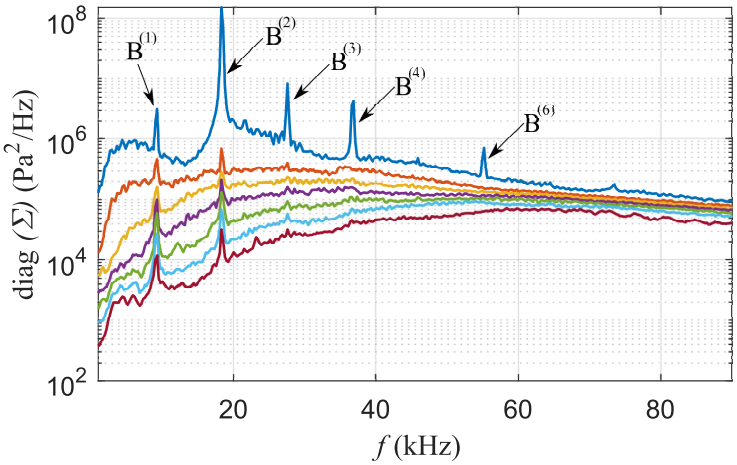

Fig. 13 Ranked odd-numbered singular values from matrix $\Sigma_{ff,T}$ for the underexpanded jet. Highest to lowest $(1, 3, 5, \ldots, 13)$ singular value plots are shown from top to bottom.

and PFD techniques, the fixed reference microphone is removed and the signal from its position is estimated through a minimization (CSMC) or a phase reference (PFD) approach. The red lines plot the corresponding coherences. The reference microphones are selected to be near the peak emission of the respective tones (microphone 3, $\theta = 90°$, for $B^{(2)}$; microphone 9, $\theta = 66°$, for $B^{(1)}$). It is noted that both CSMC and PFD methods yield excellent reconstructions of the coherence.

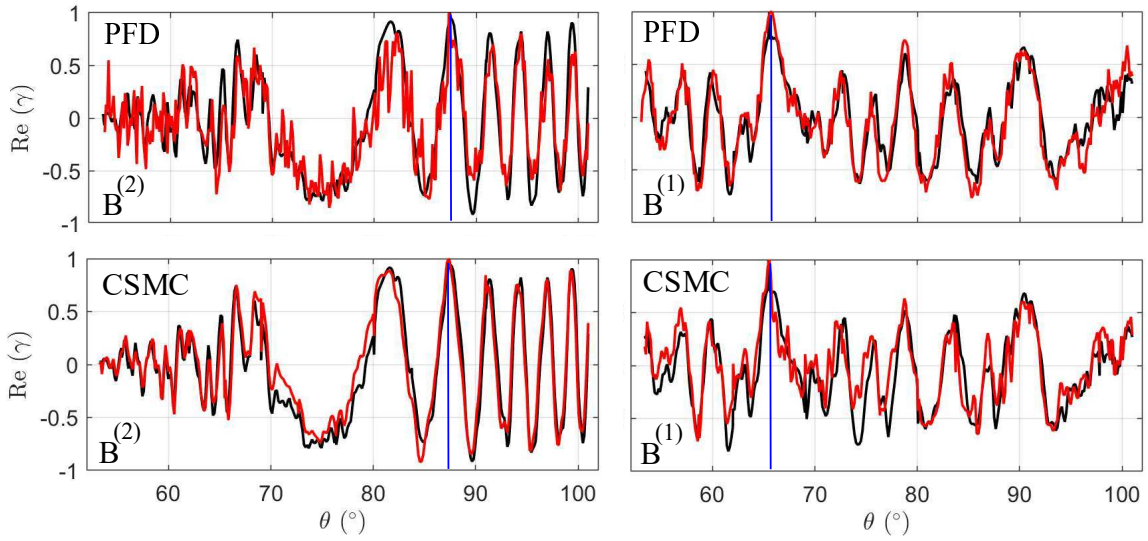

Fig. 14 Real part of the complex coherence along the microphone array line for tones $B^{(1)}$ and $B^{(2)}$ (top and bottom rows) using the CSMC and PFD methods (left and right columns) Reference positions are marked by blue vertical lines. Black lines plot the actual coherence using a physical microphone at the reference position. Red lines plot the results of obtained from the CSMC and PFD methods without a physical sensor at the reference location.

Beamforming results are shown in Fig. 15. The nozzle exit plane is located at $x = 0$ m. The noise source map obtained with fixed sensors only is highly distorted by the sidelobes and thus is of limited value. The continuous-scan paradigm greatly increases the fidelity of the beamformed maps. The CSSM, CMSC, amd PFD techniques yield similar maps that are practically devoid of sidelobe contamination. The beamformed map extends to $x/D \approx 20$ at low frequency and becomes more compact with increasing frequency, as has been observed in numerous past studies of turbulent jets (e.g., [2]). Horizontal thin layers containing periodic-like patterns represent the location of screech tones $B^{(1)}$ through $B^{(4)}$. A weak source around $x = 0$ m is seen near 9 kHz in the continuous-scan maps, indicating the interaction of upstream-propagating waves of tone $B^{(1)}$ with the nozzle lip.

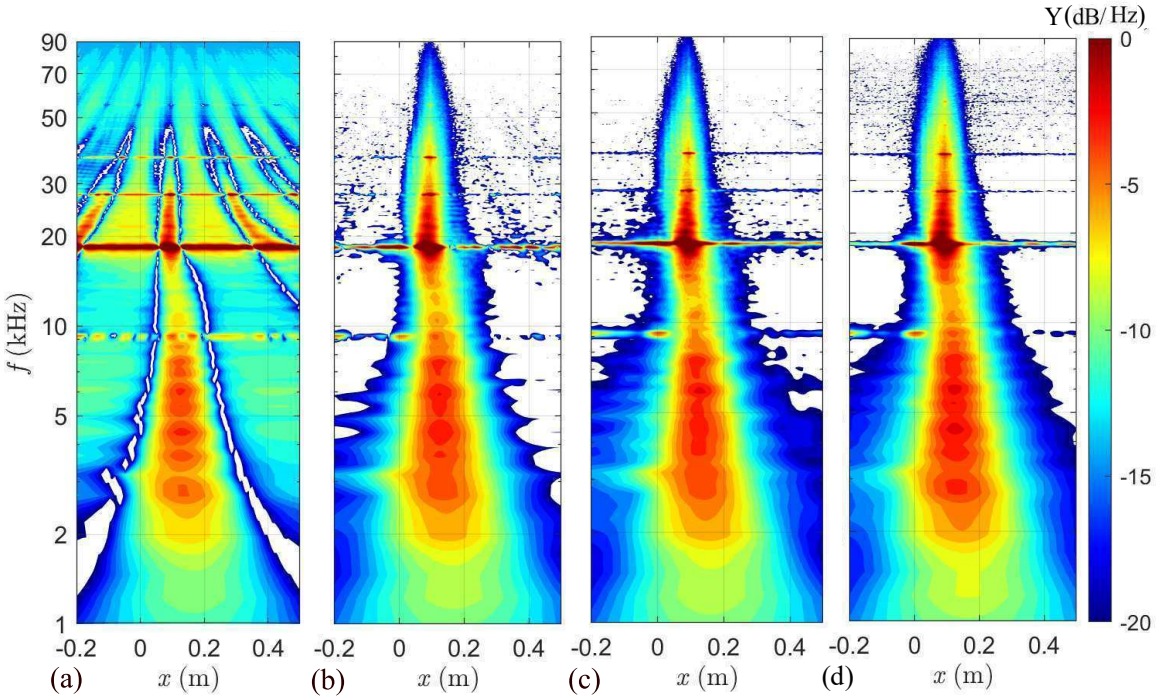

Fig. 15 Array output for the underexpanded jet. (a) FS; (b) CSSM; (c) CSMC; (d) PFD.

Although the beamformed maps using the continuous-scan approach are already of high quality, deconvolution may still be applied to further sharpen the noise source distributions. Predictably, deconvolution of the array output using fixed sensors (Fig. 15(a)) fails to provide a meaningful result due to the highly complex PSF; hence, results are shown only for the methods using the scanning microphone. Figure 16 presents the deconvolution of the array output obtained via PFD using the DAMAS, RL and CLEAN-SC algorithms. Deconvolution of the CSMC output is similar and will be shown later in a detailed assessment of the shock sources. The source now becomes highly localized and the small-scale spatial features of the jet flow are very well-resolved. It is instructive to examine the source distribution around tones $B^{(1)}$, $B^{(2)}$, $B^{(3)}$ and $B^{(4)}$, marked with horizontal lines in the DAMAS map. Reflection from the nozzle lip near $x = 0$ m, associated with the upstream-propagating waves closing the feedback mechanism loop, is visible for

$B^{(1)}$ and $B^{(2)}$ for all the maps. This effect is impossible to discern using the fixed sensors only. The location of the source peak for tones $B^{(2)}$, $B^{(3)}$ and $B^{(4)}$ lies in $5.9 \leq x/D \leq 6.25$. This apparent location is $1D$ downstream of the location from which the upstream-travelling waves were identified to be originated from for mode B by Powell *et al.* [61], and Mercier *et al.* [26], but is in line with previous experimental beamforming results of the authors (Ref. [62]).

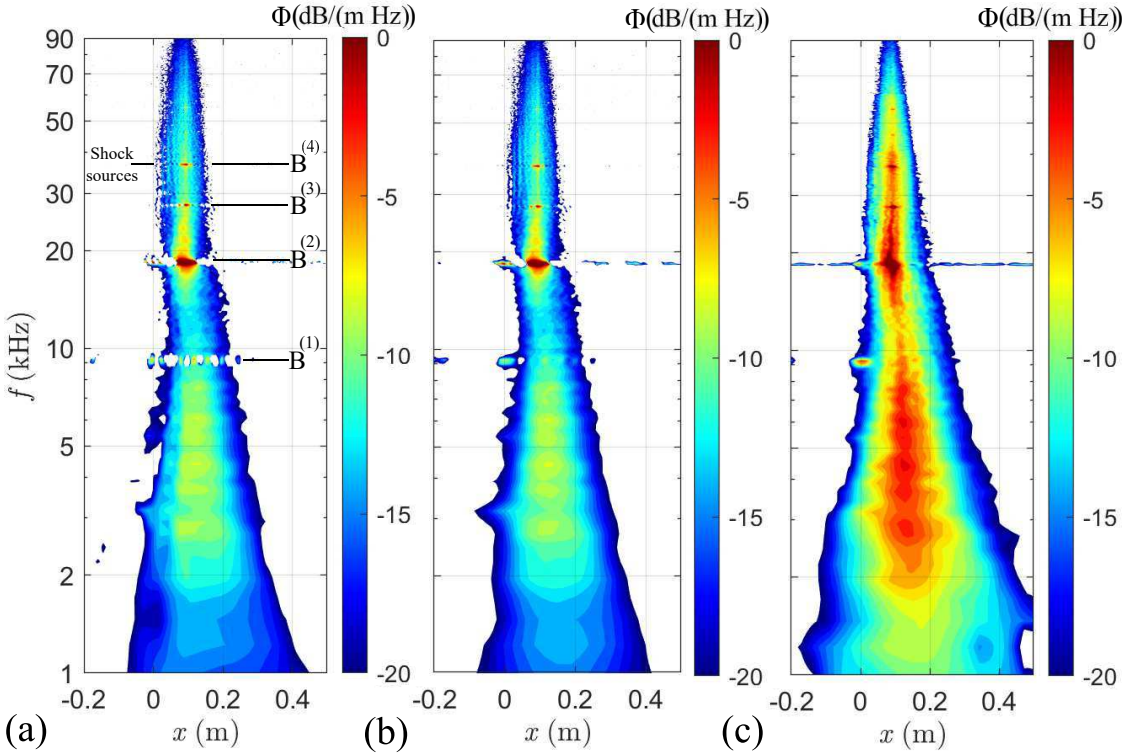

Fig. 16 Deconvolution of the PFD array output. (a) DAMAS; (b) RL; (c) CLEAN-SC.

Close examination of the deconvolved noise source maps reveals periodic vertical streaks in the frequency range of $30 \leq f \leq 50$ kHz. To study them in detail, Fig. 17 focuses on this frequency range and displays the source distributions obtained via deconvolution of the PFD (left column) and CSMC (right column) outputs using RL (first row), DAMAS (second row), and CLEAN-SC (third row). A dynamic range of 12 dB is used, and the local maximum is set to 0 dB. The colormap used in the figure has been changed with respect to the previous contours to aid the visualization of the results. The vertical patterns are discernible to about $x/D = 7$ and represent "shock sources" associated with the interaction of turbulent eddies with the shock cell structure of the jet [63]. RL and DAMAS yield fairly sharp images in this region, while the result of CLEAN-SC appears smeared. The black dashed vertical lines display the approximate location of the peak source, obtained by finding the local maxima near $35 \leq f \leq 45$ kHz in the RL and DAMAS images. It appears that the shock sources are better separated when using CSMC compared to PFD (notice the difference between the peaks and valleys of the source distribution near the second and third shock sources). It

is inferred from the figure that the shock cell spacing, which is approximately the same as the spacing of the shock sources, is between $1.17D$ and $1.20D$. This shock cell spacing is close to the wavelength of $1.20D$ of a lobed intensity pattern detected in schlieren images of an underexpanded jet with $M_j = 1.37$ by Mercier *et al.* [26]. A similar shock spacing was inferred from the coherence-based noise source maps of Ref. [62]. This underscores the high degree of spatial resolution that is attained with the continuous-scan paradigm in conjunction with DAMAS and RL, enabling the resolution of the fine scale patterns of the jet flow using far-field non-intrusive measurements. The images deconvolved with CLEAN-SC do not clearly delimit the shock sources due to the low performance of the method at separating closely-spaced sources [54].

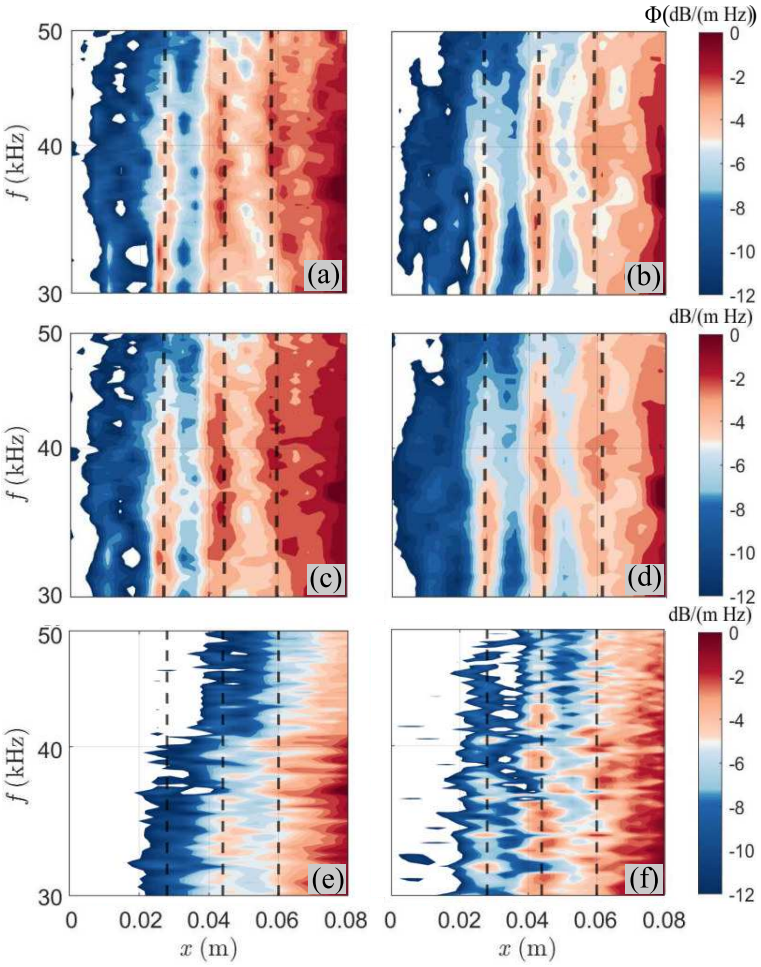

Fig. 17 Detail of the shock cell pattern around tone $B^{(4)}$ obtained via deconvolution of the PFD (left column) and CSMC (right column) outputs using RL (first row), DAMAS (second row), and CLEAN-SC (third row).

V. Conclusions

The paper adapted the delay-and-sum beamforming method and related deconvolution techniques for microphone phased arrays comprising fixed and continuously-scanning sensors. The processing of the non-stationary signals introduced by the scanning sensors requires division of all signals into quasi-stationary blocks and application of a frequency-dependent window within each block. The motion of the sensors also requires modification of the steering vectors to include a Doppler-shifted frequency. Three distinct approaches were developed to obtain the noise source maps. The first entails a direct application of delay-and-sum to each block of the divided signals followed by assembly of the outputs of the blocks. It relies on the individual cross-spectral submatrices (CSSM) of each block. The CSSM method lacks a complete cross-spectral matrix that would enable a straight-forward adoption of existing deconvolution methods. A cross-spectral matrix completion and a partial fields decomposition method are also introduced in order to use deconvolution processes. The matrix completion technique, originally implemented for non-synchronous array measurements, was adapted here to the continuous-scan approach. The partial fields decomposition method has been used in the past in near-field acoustic holography and beamforming studies. Deconvolution techniques encompassed DAMAS, Richardson-Lucy, and CLEAN-SC.

The methodologies were applied to a synthetic noise source and to a supersonic underexpanded jet that presented the phenomenon of screech. Introduction of a single scanning sensor to a far-field array comprising 13 fixed sensors improved dramatically the fidelity of beamforming. Using the DAMAS or Richardson-Lucy algorithms, the deconvolved images of the jet noise source resolved fine shock-cell features whose dimensions are similar to those imaged by optical techniques in past investigations. The CLEAN-SC deconvolution produced a reasonable overall map but could not resolve the aforementioned fine details. It is expected that utilization of the high-resolution versions of CLEAN-SC (HR-CLEAN-SC and EHR-CLEAN-SC) would allow the possibility of separating sources in close proximity given the low sidelobe levels [55, 64] attained with the dense arrays obtained using CSMC and PFD.

VI. Acknowledgments

This work was supported by Phase II Small Business Innovation Research (SBIR) contract 80NSSC20C0089 under technical monitor Dr. David Stephens of NASA GRC. ATA Engineering, Inc. was the prime.

References

[1] Billingsley, J., and Kinns, R., "The Acoustic Telescope," *Journal of Sound and Vibration*, Vol. 48, No. 4, 1976, pp. 485–510. doi:10.1016/0022-460X(76)90552-6.

[2] Venkatesh, S. R., Polak, D. R., and Narayanan, S., "Beamforming Algorithm for Distributed Source Localization and Its Application to Jet Noise," *AIAA Journal*, Vol. 41, No. 7, 2003, pp. 1238–1246. doi:10.2514/2.2092.

[3] Papamoschou, D., "Imaging of Distributed Directional Noise Sources," *Journal of Sound and Vibration*, Vol. 330, No. 10, 2011, pp. 2265–2280. doi:10.1016/j.jsv.2010.11.025.

[4] Brooks, T. F., and Humphreys, W. M., "A Deconvolution Approach for the Mapping of Acoustic Sources (DAMAS) Determined from Phased Microphone Arrays," *Journal of Sound and Vibration*, Vol. 294, No. 4, 2006, pp. 856 – 879. doi:10.1016/j.jsv.2005.12.046.

[5] Sijtsma, P., "CLEAN Based on Spatial Source Coherence," *International Journal of Aeroacoustics*, Vol. 6, No. 4, 2007, pp. 357–374. doi:10.1260/147547207783359459.

[6] Dougherty, R., "Extensions of DAMAS and Benefits and Limitations of Deconvolution in Beamforming," *AIAA Paper 2005-2961*, 2005. doi:10.2514/6.2005-2961.

[7] Merino-Martinez, R., Sijtsma, P., Snellen, M., Ahlefeldt, T., Antoni, J., Bahr, C., Blacodon, D., Ernst, D., Finez, A., Funke, S., Geyer, T., Haxter, S., Herold, G., Huang, X., Humphreys, W., Leclere, Q., Malgoezar, A., Michel, U., Padois, T., Pereira, A., Picard, C., Sarradj, E., Siller, J., Simons, D., and Spehr, C., "A Review of Acoustic Imaging Methods Using Phased Microphone Arrays," *CEAS Aeronautical Journal*, Vol. 10, 2019, p. 197–230. doi:10.1007/s13272-019-00383-4.

[8] Merino-Martínez, R., Luesutthiviboon, S., Zamponi, R., Rubio Carpio, A., Ragni, D., Sijtsma, P., Snellen, M., and Schram, C., "Assessment of the Accuracy of Microphone Array Methods for Aeroacoustic Measurements," *Journal of Sound and Vibration*, Vol. 470, 2020, p. 115176. doi:doi.org/10.1016/j.jsv.2020.115176.

[9] Bahr, C. J., Humphreys, W. M., Ernst, D., Ahlefeldt, T., Spehr, C., Pereira, A., Leclère, Q., Picard, C., Porteous, R., Moreau, D., Fischer, J. R., and Doolan, C. J., "A Comparison of Microphone Phased Array Methods Applied to the Study of Airframe Noise in Wind Tunnel Testing," *AIAA Paper 2017-3718*, 2017. doi:10.2514/6.2017-3718.

[10] Arcondoulis, E., and Liu, Y., "An Iterative Microphone Removal Method for Acoustic Beamforming Array Design," *Journal of Sound and Vibration*, Vol. 442, 2019, pp. 552–571. doi:10.1016/j.jsv.2018.11.005.

[11] Lee, M., and Bolton, J. S., "Source Characterization of a Subsonic Jet by Using Near-Field Acoustical Holography," *The Journal of the Acoustical Society of America*, Vol. 121, No. 2, 2007, pp. 967–977. doi:10.1121/1.2404626.

[12] Vold, H., Shah, P., Davis, J., Bremner, P., McLaughlin, D., Morris, P., Veltin, J., and McKinley, R., "High Resolution Continuous Scan Acoustical Holography Applied to High-Speed Jet Noise," *AIAA Paper 2010-3754*, 2010. doi:10.2514/6.2010-3754.

[13] Shah, P., Vold, H., and Yang, M., "Reconstruction of Far-Field Noise Using Multireference Acoustical Holography Measurements of High-Speed Jets," 2011. doi:10.2514/6.2011-2772.

[14] Li, L., Wang, S., Li, F., Zheng, X., Wu, Y., Gao, Y., and Qiao, Y., "Three-dimensional localization of gas leakage using acoustic holography," *Mechanical Systems and Signal Processing*, Vol. 171, 2022, p. 108952. doi:10.1016/j.ymssp.2022.108952.

[15] Stephens, D. B., and Vold, H., "Order tracking signal processing for open rotor acoustics," *Journal of Sound and Vibration*, Vol. 333, No. 16, 2014, pp. 3818 – 3830. doi:https://doi.org/10.1016/j.jsv.2014.04.005.

[16] Comesana, D. F., Holland, K. R., Escribano, D. G., and de Bree, H.-E., "An Introduction to Virtual Phased Arrays for Beamforming Applications," *Archives of Acoustics*, Vol. vol. 39, 2014, pp. 81–88. doi:10.2478/aoa-2014-0009.

[17] Nicolas, F., and Rey, M., "S1MAWind Tunnel New Aeroacoustic Capability: a Traversing Microphone Array," *AIAA Paper 2018-3137*, 2018. doi:10.2514/6.2018-3137.

[18] Shah, P., Vold, H., Hensley, D., Envia, E., and Stephens, D., "A High-Resolution Continuous-Scan Acoustic Measurement Method for Turbofan Engine Applications," *Journal of Turbomachinery*, Vol. 137, 2015, pp. 121002–121002–11. doi: 10.1115/1.4031341.

[19] Papamoschou, D., Morata, D., and Shah, P., "Inverse Acoustic Methodology for Continuous-Scan Phased Arrays," *AIAA Journal*, Vol. 57, No. 12, 2019, pp. 5126–5141. doi:10.2514/1.J058085.

[20] Morata, D., and Papamoschou, D., "Advances in the Direct Spectral Estimation of Aeroacoustic Sources Using Continuous-Scan Phased Arrays," *AIAA Paper 2021-0215*, 2021. doi:10.2514/6.2021-0215.

[21] Yu, L., Antoni, J., Wu, H., Leclere, Q., and Jiang, W., "Fast Iteration Algorithms for Implementing the Acoustic Beamforming of Non-Synchronous Measurements," *Mechanical Systems and Signal Processing*, Vol. 134, 2019, p. 106309. doi:10.1016/j.ymssp.2019.106309.

[22] Yu, L., Guo, Q., Chu, N., and Wang, R., "Achieving 3D Beamforming by Non-Synchronous Microphone Array Measurements," *Sensors*, Vol. 20, No. 24, 2020. doi:10.3390/s20247308.

[23] Ning, F., Song, J., Hu, J., and Wei, J., "Sound Source Localization of Non-Synchronous Measurements Beamforming with Block Hermitian Matrix Completion," *Mechanical Systems and Signal Processing*, Vol. 147, 2021, p. 107118. doi: 10.1016/j.ymssp.2020.107118.

[24] Hu, D., Ding, J., Zhao, H., and Yu, L., "Spatial Basis Interpretation for Implementing the Acoustic Imaging of Non-Synchronous Measurements," *Applied Acoustics*, Vol. 182, 2021, p. 108198. doi:10.1016/j.apacoust.2021.108198.

[25] Lima Pereira, L. T., Merino-Martínez, R., Ragni, D., Gómez-Ariza, D., and Snellen, M., "Combining Asynchronous Microphone Array Measurements for Enhanced Acoustic Imaging and Volumetric Source Mapping," *Applied Acoustics*, Vol. 182, 2021, p. 108247. doi:10.1016/j.apacoust.2021.108247.

[26] Mercier, B., Castelain, T., and Bailly, C., "Experimental Characterisation of the Screech Feedback Loop in Underexpanded Round Jets," *Journal of Fluid Mechanics*, Vol. 824, 2017, p. 202–229. doi:10.1017/jfm.2017.336.

[27] Gojon, R., and Bogey, C., "Numerical Study of th Flow and the Near Acoustic Fields of an Underexpanded Round Free Jet Generating Two Screech Tones," *International Journal of Aeroacoustics*, Vol. 16, No. 7-8, 2017, pp. 603–625. doi: 10.1177/1475472X17727606.

[28] Edgington-Mitchell, D., "Aeroacoustic Resonance and Self-Excitation in Screeching and Impinging Supersonic Jets – A Review," *International Journal of Aeroacoustics*, Vol. 18, No. 2-3, 2019, pp. 118–188. doi:10.1177/1475472X19834521.

[29] Li, X.-R., Zhang, X.-W., Hao, P.-F., and He, F., "Acoustic Feedback Loops for Screech Tones of Underexpanded Free Round Jets at Different Modes," *Journal of Fluid Mechanics*, Vol. 902, 2020. doi:10.1017/jfm.2020.436.

[30] Chakrabarti, S., Gaitonde, D., and Unnikrishnan, S., "Representing Rectangular Jet Dynamics Through Azimuthal Fourier Modes," *Phys. Rev. Fluids*, Vol. 6, 2021, p. 074605. doi:10.1103/PhysRevFluids.6.074605.

[31] Chakrabarti, S., Gaitonde, D. V., and Unnikrishnan, S., "Wavepacket Dynamics in Rectangular Jets," *AIAA Paper 2022-2403*, 2022. doi:10.2514/6.2022-2403.

[32] Morata, D., and Papamoschou, D., "Extension of Traditional Beamforming Methods to the Continuous-Scan Paradigm," *AIAA Paper 2022-1154*, 2022. doi:10.2514/6.2022-1154.

[33] Dougherty, R., "Functional Beamforming," *Berlin Beamforming Conference*, 2014.

[34] Merino-Martínez, R., Snellen, M., and Simons, D. G., "Functional Beamforming Applied to Imaging of Flyover Noise on Landing Aircraft," *Journal of Aircraft*, Vol. 53, No. 6, 2016, pp. 1830–1843. doi:10.2514/1.C033691.

[35] Hald, J., "Cross-Spectral Matrix Diagonal Reconstruction," *Inter-Noise and Noise-Con Conference*, Vol. 253, No. 5, 2016, pp. 3766–3777.

[36] Dougherty, R., "Cross-Spectral Matrix Diagonal Optimization," *Berlin Beamforming Conference (BeBeC)*, 2016.

[37] Grant, M., and Boyd, S., "Graph implementations for nonsmooth convex programs," *Recent Advances in Learning and Control*, edited by V. Blondel, S. Boyd, and H. Kimura, Lecture Notes in Control and Information Sciences, Springer-Verlag Limited, 2008, pp. 95–110. `http://stanford.edu/~boyd/graph_dcp.html`.

[38] Grant, M., and Boyd, S., "CVX: Matlab Software for Disciplined Convex Programming, version 2.1," `http://cvxr.com/cvx`, Mar. 2014.

[39] Dinsenmeyer, A., Antoni, J., Leclère, Q., and Pereira, A., "A probabilistic approach for cross-spectral matrix denoising: Benchmarking with some recent methods," *The Journal of the Acoustical Society of America*, Vol. 147, No. 5, 2020, pp. 3108–3123. doi:10.1121/10.0001098.

[40] Leclère, Q., "Multi-Channel Spectral Analysis of Multi-Pass Acquisition Measurements," *Mechanical Systems and Signal Processing*, Vol. 23, No. 5, 2009, pp. 1415–1422. doi:10.1016/j.ymssp.2008.12.002.

[41] Antoni, J., Liang, Y., and Leclère, Q., "Reconstruction of sound quadratic properties from non-synchronous measurements with insufficient or without references: Proof of concept," *Journal of Sound and Vibration*, Vol. 349, 2015, pp. 123–149. doi:10.1016/j.jsv.2015.03.008.

[42] Yu, L., Antoni, J., and Leclere, Q., "Spectral Matrix Completion by Cyclic Projection and Application to Sound Source Reconstruction from Non-Synchronous Measurements," *Journal of Sound and Vibration*, Vol. 372, 2016, pp. 31–49. doi: 10.1016/j.jsv.2016.02.031.

[43] Yu, L., Antoni, J., Leclere, Q., and Jiang, W., "Acoustical Source Reconstruction from Non-Synchronous Sequential Measurements by Fast Iterative Shrinkage Thresholding Algorithm," *Journal of Sound and Vibration*, Vol. 408, 2017, pp. 351–367. doi:10.1016/j.jsv.2017.07.036.

[44] Goates, C. B., Harker, B. M., Neilsen, T. B., and Gee, K. L., "Extending the Bandwidth of an Acoustic Beamforming Array Using Phase Unwrapping and Array Interpolation," *The Journal of the Acoustical Society of America*, Vol. 141, No. 4, 2017, pp. 407–412. doi:10.1121/1.4981235.

[45] Yu, L., "Acoustical Source Reconstruction from Non-Synchronous Sequential Measurements," *PhD Thesis - INSA de Lyon*, 2015.

[46] Shah, P. N., White, A., Hensley, D., Papamoschou, D., and Vold, H., "Continuous-Scan Phased Array Measurement Methods for Turbofan Engine Acoustic Testing," *Journal of Engineering for Gas Turbines and Power*, Vol. 141, No. 8, 2019. doi: 10.1115/1.4042395.

[47] Shah, P. N., and Papamoschou, D., "Characterization of High Speed Jet Acoustics Using High-Resolution Multi-Reference Continuous-Scan Acoustic Measurements on a Linear Array," *AIAA Paper 2020-0005*, 2020. doi:10.2514/6.2020-0005.

[48] Lee, A., Shah, P., White, A., Hensley, D., and Schweizer, L., "Continuous-Scan Beamforming for Identification of Highly Varying Amplitude Sources with Low Sensor Budgets," *Berlin Beamforming Conference*, 2020.

[49] Nam, K.-U., and Kim, Y.-H., "A Partial Field Decomposition Algorithm and its Examples for Near-Field Acoustic Holography," *The Journal of the Acoustical Society of America*, Vol. 116, No. 1, 2004, pp. 172–185. doi:10.1121/1.1756896.

[50] Lee, M., and Bolton, J. S., "Scan-Based Near-Field Acoustical Holography and Partial Field Decomposition in the Presence of Noise and Source Level Variation," *The Journal of the Acoustical Society of America*, Vol. 119, No. 1, 2006, pp. 382–393. doi:10.1121/1.2133717.

[51] Richardson, W. H., "Bayesian-Based Iterative Method of Image Restoration," *Journal of the Optical Society of America*, Vol. 62, No. 1, 1972, pp. 55–59. doi:10.1364/JOSA.62.000055.

[52] Lucy, L., "An Iterative Technique for the Rectification of Observed Distributions," *Astronomical Journal*, Vol. 79, 1974, p. 745. doi:10.1086/111605.

[53] Tiana-Roig, E., and Jacobsen, F., "Deconvolution for the Localization of Sound Sources Using a Circular Microphone Array," *The Journal of the Acoustical Society of America*, Vol. 134, No. 3, 2013, pp. 2078–2089. doi:10.1121/1.4816545.

[54] de Santana, L., "Fundamentals of Acoustic Beamforming," *NATO Educational Notes EN-AVT-287-04*, 2017.

[55] Luesutthiviboon, S., Malgoezar, A. M., Merino-Martinez, R., Snellen, M., Sijtsma, P., and Simons, D. G., "Enhanced HR-CLEAN-SC for Resolving Multiple Closely Spaced Sound Sources," *International Journal of Aeroacoustics*, Vol. 18, No. 4-5, 2019, pp. 392–413. doi:10.1177/1475472X19852938.

[56] Sushil, S. K., Garg, M., and Narayanan, S., "Estimation of the lower cut-off frequency of an anechoic chamber: An empirical approach," *International Journal of Aeroacoustics*, Vol. 19, No. 1-2, 2020, pp. 57–72. doi:10.1177/1475472X20905070.

[57] Steinberg, B. D., "Principles of Aperture and Array System Design: Including Random and Adaptive Arrays," *New York, Wiley-Interscience*, 1976.

[58] Seiner, J. M., Manning, J. C., and Ponton, M. K., "Dynamic Pressure Loads Associated with Twin Supersonic Plume Resonance," *AIAA Journal*, Vol. 26, No. 8, 1988, pp. 954–960. doi:10.2514/3.9996.

[59] Tam, C. K., Parrish, S. A., and Viswanathan, K., "The Harmonics of Jet Screech Tones," *AIAA Paper 2013-2091*, 2013. doi:10.2514/6.2013-2091.

[60] Norum, T. D., "Screech Suppression in Supersonic Jets," *AIAA Journal*, Vol. 21, No. 2, 1983, pp. 235–240. doi:10.2514/3.8059.

[61] Powell, A., Umeda, Y., and Ishii, R., "Observations of the Oscillation Modes of Choked Circular Jets," *The Journal of the Acoustical Society of America*, Vol. 92, No. 5, 1992, pp. 2823–2836. doi:10.1121/1.404398.

[62] Morata, D., and Papamoschou, D., "Effect of Nozzle Geometry on the Space-Time Emission of Screech Tones," *AIAA Paper 2021-2306*, 2021. doi:10.2514/6.2021-2306.

[63] Breen, N. P., and Ahuja, K. K., "Limitations of Acoustic Beamforming for Accurate Jet Noise Source Location," *AIAA Paper 2020-2603*, 2020. doi:10.2514/6.2020-2603.

[64] Sijtsma, P., Merino-Martinez, R., Malgoezar, A. M., and Snellen, M., "High-resolution CLEAN-SC: Theory and experimental validation," *International Journal of Aeroacoustics*, Vol. 16, No. 4-5, 2017, pp. 274–298. doi:10.1177/1475472X17713034.